ALMA MATER STUDIORUM
UNIVERSITA' DI BOLOGNA

SCHOOL OF ENGINEERING

-Forlì Campus-

SECOND CYCLE MASTER's DEGREE in
AEROSPACE ENGINEERING
Class: LM-20

GRADUATION THESIS in:
Spacecraft Attitude Dynamics and Control

Design of Thrust Vectoring attitude control system for Lunar Lander flying testbed

CANDIDATE
David Bernacchia

SUPERVISOR
Prof. Marco Zannoni

CO-SUPERVISOR
Prof. David Barnhart

V Session
Academic year 2018/2019

Abstract

The proposed work has been developed within the project LEAPFROG (Lunar Entry and Approach Platform For Research On Ground) at the University of Southern California. The project concerns the realization of a lunar lander test bed prototype with the aim of testing GNC algorithms for simulated lunar flight and descent. The main focus is the realization of a newly designed thrust vectoring system (TVC) that exploits the thrust given by a main engine in order to control the attitude of the platform. This new attitude control system is combined with current tradtional reaction control system (RCS) based on cold-gas thrusters. After a preliminary hardware design phase, a linear LQR controller, based on a reduced quaternion model, and a non-linear sliding mode controller are designed for the TVC system. Linear Quadratic Regulator offers a simple implementation, an optimal control law. However it can be affected by un-modeled dynamics and the solutions provided are, in general, only locally valid. Sliding mode control (SMC) guarantees robustness against disturbances, unmodeled dynamics and uncertainties about the mass properties of the prototype, offering also a global stability. Cons of this method are the hard implementation and the request of an high-frequency actuation. A MATLAB/simulink simulation is set up in order to validate and compare the designed controllers and to analyze if the thrust vectoring system leads to the desired results.

Contents

1 Introduction **1**

1.1 Introduction to LEAPFROG project 1

1.2 Generation 2: proposal and goals 3

1.3 Thesis work and outline 4

2 Theoretical background **7**

2.1 Landing on a celestial body 7

2.2 Frames of reference 9

2.3 Attitude representation 10

2.3.1 Euler Angles representation 11

2.3.2 Quaternions representation 12

2.4 Attitude kinematics 13

2.5 Rigid body attitude dynamics 15

2.6 Thrust vector control: literature review 17

2.6.1 Reactive fluid injection 17

2.6.2 Exhaust flow deflection 18

2.6.3 Engine mechanical manipulation 19

3 Preliminary hardware design **23**

3.1 Project budget and requirements 23

3.2 Structure 23

3.2.1 Chassis 25

3.2.2 Legs 26

3.2.3 Platforms 26

3.3 Propulsion system 27

3.4 Reaction control system 28

3.5 Thrust Vector Control system 30

3.5.1 Gimbal joint design 33
3.5.2 Actuation system 35
3.5.3 Embedded electronics 39

4 Control system design **41**
4.1 System Dynamics 41
4.2 Linear Quadratic Regulator 44
4.2.1 Cost function and Riccati equation 45
4.2.2 Reduced quaternion model 47
4.2.3 Asymptotic stability 49
4.3 Sliding Mode Control 50
4.3.1 Sliding manifold and control law definition 51
4.3.2 Chattering phenomenon 53

5 Control system simulation **57**
5.1 Input parameters 57
5.2 LQR controller simulations 58
5.2.1 Ideal case 60
5.2.2 Perturbed case 62
5.3 Sliding mode controller simulations 72
5.3.1 Ideal case 73
5.3.2 Perturbed case 75

Conclusions and future work **84**

Appendix A **85**

Bibliography **88**

Acknowledgements **89**

List of Figures

Figure 1.1 The Lunar Landing Research Vehicle 2
Figure 1.2 LEAPFROG generation 1 (CAD model) 3
Figure 2.1 Apollo lunar landing sequence [7] 8
Figure 2.2 Frames of reference adopted 9
Figure 2.3 Reactive flow injection on TitanIIIE-Centaur (NASA) [1] . . . 18
Figure 2.4 Example of gimbaled thrust on a rocket [6] 19
Figure 2.5 Typical joints used on gimbaled engines [10] 20
Figure 2.6 LLRV gimbaled engine [20] 21
Figure 3.1 Structure of Generation 2 - CAD model (front view) 24
Figure 3.2 Structure of Generation 2 - CAD model (top view) 24
Figure 3.3 Carbon fiber chassis - final version 25
Figure 3.4 JetCat P300 PRO [2] 27
Figure 3.5 RCS thrusters placement 28
Figure 3.6 RCS block diagram 30
Figure 3.7 Conceptual sketch of the gimbal ring 33
Figure 3.8 Gimbal ring mechanical design 34
Figure 3.9 Windynation linear actuator [33] 35
Figure 3.10 Actuators: speed vs load [33] 36
Figure 3.11 Actuators installation scheme 38
Figure 3.12 Thrust vectoring system embedded electronics 39
Figure 3.13 LEAPFROG Generation 2 40
Figure 4.1 Thrust vector decomposition 43
Figure 4.2 Ideal sliding mode [13] 50
Figure 4.3 Chattered sliding mode [12] 54
Figure 5.1 Pitch angle control 60
Figure 5.2 Pitch rate control 61
Figure 5.3 Gimbal offset angle δ 61

Figure 5.4 Gimbal rotation angle ξ 62
Figure 5.5 Half-sine unitary impulse 63
Figure 5.6 Pitch channel 63
Figure 5.7 angle δ - impulse response (pitch) 64
Figure 5.8 angle δ - impulse response (pitch and yaw) 64
Figure 5.9 angle ξ - impulse response (pitch and yaw) 65
Figure 5.10 Yaw channel - external random noise 66
Figure 5.11 Pitch channel - external random noise 66
Figure 5.12 Angle δ in presence of random noise 67
Figure 5.13 Angle ξ in presence of random noise 67
Figure 5.14 Displacement linear actuator 1 68
Figure 5.15 Displacement linear actuator 2 68
Figure 5.16 Yaw channel - presence of state measurements errors 69
Figure 5.17 Pitch channel - presence of state measurements errors 69
Figure 5.18 Pitch angle - different scenarios 70
Figure 5.19 Yaw angle - different scenarios 71
Figure 5.20 Gimbal offset angle - different scenarios 71
Figure 5.21 Chattered phase plane 73
Figure 5.22 Pitch angle and pitch rate behaviour under sliding mode control 74
Figure 5.23 Angle δ under sliding mode control 74
Figure 5.24 Pitch channel - impulse disturbance 75
Figure 5.25 Yaw channel - impulse disturbance 75
Figure 5.26 Gimbal offset angle - combined pulses disturbances 76
Figure 5.27 Gimbal rotation angle - combined pulses disturbances 76
Figure 5.28 Displacement linear actuator 1 - pulse disturbance 77
Figure 5.29 Displacement linear actuator 2 - pulse disturbance 77
Figure 5.30 Pitch and yaw angles - random disturbance 78
Figure 5.31 Displacement linear actuator 1 - random disturbance 78
Figure 5.32 Displacement linear actuator 2 - random disturbance 79
Figure 5.33 Pitch angle fluctuation due to measurements errors 79
Figure 5.34 Pitch angle - different scenarios 80
Figure 5.35 Yaw angle - different scenarios 80
Figure 5.36 Gimbal offset angle - different scenarios 81

Chapter 1

Introduction

1.1 Introduction to LEAPFROG project

In the last few years, lunar exploration has been experiencing a new "golden age", after the intense period of interest from the well-known Apollo missions. News from the recent Chandrayaan-2 mission by Indian Space Research Organisation and NASA's 2024 goal to bring back humans to the Moon's surface, Moon exploration and lunar landing are of great interest not only for big national or international agencies, like NASA or ESA, but also for private companies, research centers and universities. University of Southern California's (USC) Space Engineering Research Center (SERC), with the support from the Information Sciences Institute (ISI), started its personal research in prototype lunar lander technology in 2006, with the birth of the LEAPFROG project.

LEAPFROG (Lunar Entry and Approach Platform For Research On Ground) is a lunar lander prototype built by students with the aim of simulating lunar gravity on Earth. Since the very beginning, the main goal of the project has been the development of a test bed lunar prototype vehicle that can fly multiple times in Earth's gravity through free flight to simulate a lunar descent and landing sequence. The concept was inspired by NASA's Lunar Landing Research Vehicle (LLRV), created to investigate and analyze different piloting techniques that could be used for the descent and landing of the Apollo Lunar Module [5]. The LLRV project, in fact, was started even before NASA had selected the landing strategies to use for the Lunar Module (LM). The LLRV led to the Lunar Landing Training Vehicle (LLTV), a vehicle designed with characteristics closer to the planned LM, to better represent the final descent phase, used for a more advanced training of the Apollo astronauts [20].

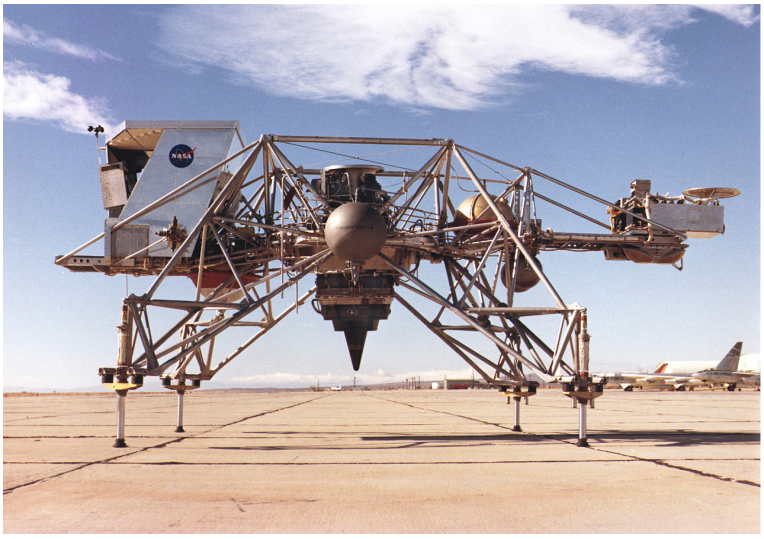

Figure 1.1: The Lunar Landing Research Vehicle

From the first day, the LEAPFROG project was planned to be a multi-generational activity, where every new academic year was intended to increase the performance and capability of the simulated lander through each subsequent new generation of the vehicle. The first prototype (Generation 0) used all commercial off the shelf hardware, in order to maintain the lowest possible cost and to allow students to have a true "hands on" training in the system life cycle of a simulated space vehicle [5]. It was characterized by a a kerosene-powered JetCat P200 jet engine used for hover and descent flight, while lateral and rotational control was provided by a Reaction Control System (RCS) composed by 12 cold-gas thrusters driven by solenoid valves which regulated pulse of air with an on-off configuration. Guidance, Navigation and Control (GNC) codes were then developed in order to maintain the platform self-equilibrium, using stability measurements coming from the primary avionics sensor, an inertial measurement unit (IMU) [16]. At the end of the design and building phase, some flight tests were performed to address the behaviour of the prototype. Even if the flight tests showed some encouraging results, many issues were encountered, primarily related to a non-complete optimization of the vehicle.

A new phase for LEAPFROG started back up in 2018, starting from the goals and end results obtained in Generation 0, to build a new generation of the vehicle (Generation 1) with improved capabilities, to fix the main issues encountered with the first prototype. One of the main problems of the first vehicle was the difficulty to maintain a stabilized configuration in hover flight. For this reason the main focus of Generation 1 team was the improvement of the cold-gas thrusters based attitude control system, testing different sizes for the thrusters nozzle and designing new arms capable to increase the control torque given by the thrusters themselves. The general structure was kept almost equal to the one of the previous generation

since particular requirements in terms of payload capacity were not given for this prototype.

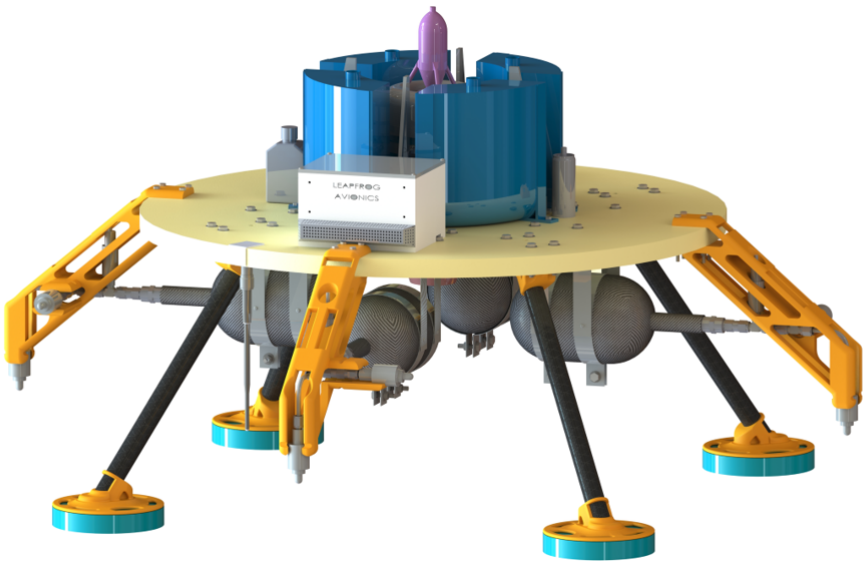

Figure 1.2: LEAPFROG generation 1 (CAD model)

1.2 Generation 2: proposal and goals

In September 2019, a new team further improved the design and subsystems of the LEAPFROG, starting Generation 2 of the project. The work, focused on additional improvements to the new generation prototype,with additional requirements:

- Increase payload capacity
- Increase thrust to weight ratio
- Increase the flight time
- Enable a more re-configurable structure
- Enable capability to withstand a free fall from up to 3 meters
- Optimize and improve subsystems and guidance algorithms
- Continue to pursue lowest possible cost
- Enable ability to perform multiple hops during the same flight test

Secondary goals were also considered for a future vehicle design that would be closer to an actual lunar lander prototype, by transitioning the current jet engine with a rocket propulsion system and integrating space-qualified hardware [5].

Starting from the primary requirements, a new structure and subsystems were designed and developed, with a planned flight test scheduled for the end of Spring 2020.

1.3 Thesis work and outline

The present thesis work was developed within the Generation 2 of the LEAPFROG project. Starting from the purpose of improving the subsystems relative to the attitude control and increase the payload capacity of the prototype, my research work concerned the design and implementation of a merged multi-control GNC system based on a newly designed thrust vector control (TVC) system, that ties into the air breathing turbine engine, that could work together with the old RCS based on cold-gas thrusters. The main idea behind the TVC system is to exploit the energy given by the main engine in order to control and balance the platform. The principal hardware of the system is characterized by a gimbal ring that allows the motion of the principal engine around a particular center of rotation. The engine is moved and oriented to the desired position by a couple of linear electro-mechanical actuators. Recalling the view of a change of the propulsion system, the design of the TVC system should work with different thrust outputs (i.e jet engine or rocket engine) and should be adaptable to different thrust values and environmental conditions. The aim of the work was to verify if, through the implementation of the TVC system, it's possible to avoid, or at least reduce, the usage of the cold-gas thrusters system, thus reducing the consumption of RCS gas. In fact, the implementation of the thrust vectoring system, not only can improve the maneuverability of the prototype, but it can also lead to a reduction of the total mass of the structure. This happens because, with an important reduction of RCS propellant consumption, we may be able to reduce the carried weight relative to the cold-gas tanks, saving mass and, consequently, increasing the payload capacity of the vehicle.

In parallel with the work on the TVC system, I collaborated, with the other team members, in the development and design of the new structure and other subsystems of the prototype.

From here on, the thesis will be composed by 4 more chapters divided as follows: the 2nd chapter will give an introduction to all the theoretical concepts behind the analysis of a rigid body's attitude and the development of an attitude control system. The 3rd chapter will describe the design phase of the new prototype, including

both the general structure and, more in detail, the hardware relative to the Thrust Vector Control system. In the 4th chapter the dynamic model of the prototype will be write down in terms of equations of motion and the theoretical design of the control system algorithms will be presented. The 5th and last chapter will show the results obtained implementing the control systems described in the 4th chapter, in a MATLAB/Simulink environment. Final conclusions will be discussed, together with the expected future works that can be done to improve the Guidance Navigation and Control system of the LEAPFROG, relative to the main goals of the project.

Chapter 2

Theoretical background

In the present chapter are presented the theoretical foundations on which the problem of attitude representation, determination and control is based. A quick review and introduction to the concepts of Thrust Vector Control and landing sequence are also given.

2.1 Landing on a celestial body

When we talk about lander spacecraft, we are referring to particular spacecrafts that are designed to reach the surface of a celestial body and be able to land successfully in order to communicate with Earth [22]. The design of the landing sequence is a crucial task for the success of a mission and the strategies used are strictly related to the characteristics and the nature of the target body and the lander. For example, a landing performed on a planet with an atmosphere would be characterized by different strategies with respect to a landing maneuver performed on an airless body, like an asteroid or the Moon. In the first case, in fact, the interaction between the atmosphere and the probe can be exploited to slow down the latter through the usage of different devices like parachutes. In the case of an airless body, since this method cannot clearly be used, the slowdown is entrusted to the propulsion system and is usually combined to other particular maneuvers. A very simple descent control strategy is the so called *gravity turn* in which the thrust vector is aligned with the velocity vector in order to cancel the initial horizontal component of the spacecraft's velocity. The continuous braking, combined with the action of the gravity, progressively changes the velocity vector, which becomes more and more dominated by the vertical component induced by the gravity itself. The simplicity of this particular maneuver is counterbalanced by its poor behaviour in terms of fuel consumption. This because, being a quite slow maneuver, the more it takes the landing the more a vertical velocity component, that has to be cancelled out by the

propulsion system, is added [4]. This particular landing strategy is called powered descent. A typical example of soft landing sequence in Moon environment is the one adopted by the Apollo missions, depicted in Figure 2.1:

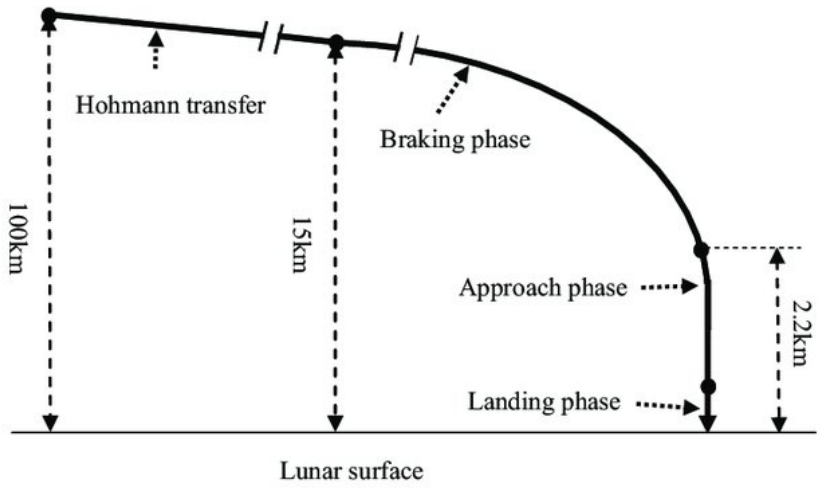

Figure 2.1: Apollo lunar landing sequence [7]

As we can see, the full maneuver is characterized by three different phases: braking phase, approach phase and landing phase. The braking phase is the first part of the powered descent and it's designed to reduce the orbital velocity of the spacecraft and, consequently, the altitude. The approach phase was designed for the pilot in order to monitor the approach to the surface of the Moon. The final landing phase starts when the altitude is strongly reduced (around 150 meters in the case of Apollo mission [7]) and should be performed with a low velocity and an attitude such that a soft vertical landing is guaranteed. During the whole landing maneuver, the attitude control is really important since the transition between the different phases should be, in terms of attitude angles, as smooth as possible.

However, thinking about lunar exploration, is clear that the possibility to analyze and have surface measurements in different locations is scientifically interesting. For this reason landers are usually designed to be able to hover and perform a so called powered re-ascent, in order to move to different spots. Without atmosphere, this may be the only way to travel long distances over the lunar surface efficiently and quickly. This type of landers that are able to take off vertically, travel and land softly again on lunar surface, are defined as Vertical Take-off Vertical Landing spacecrafts (VTVL) [7]. The LEAPFROG prototype conceptually belongs to this category of vehicles since one of its goal will be being able to perform multiple hops, landing softly each time.

In general the vertical soft landing task is much harder to achieve with respect to the vertical take-off or the travelling case, due to the many constraints in terms of

attitude angles and attitude angular velocity. This underlines the importance of the attitude control system while the landing sequence is performed.

2.2 Frames of reference

Since the work concerns the development of an attitude control system for a prototype performing a landing maneuver, the frames of reference considered are the following:

- *Body-centered frame of reference*

  The origin coincides with the center of mass of the body while the axis are directed along the principal axis of inertia. It is described by the triad $\{\hat{i}, \hat{j}, \hat{k}\}$

- *Planet-fixed frame of reference*

  This frame of reference is fixed to the planet on which the landing is performed (the Earth for LEAPFROG). The origin is placed in correspondence of the target landing spot, the $\hat{c_3}$ axis is perpendicular to the surface and aligned with the center of the Earth, the other 2 axis lay on the surface, pointing $\hat{c_1}$ towards east and $\hat{c_2}$ towards north, relative to the magnetic north. The short amount of time that takes the landing maneuver to be done allows us to neglect the rotation of the Earth and consider this frame of reference inertial. It is described by the triad $\{\hat{c_1}, \hat{c_2}, \hat{c_3}\}$

The frames of reference are depicted in the following figure:

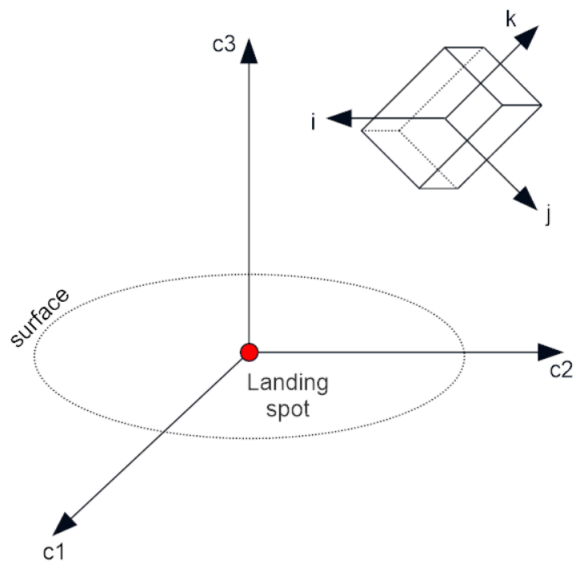

Figure 2.2: Frames of reference adopted

2.3 Attitude representation

When we face a problem of attitude representation, the fundamental concept to deal with is the description of the relative orientation between two frames of reference. This task is accomplished by writing each component of the body-fixed reference system in terms of the 3 inertial unit vectors, getting 9 scalar parameters that are usually arranged in matrix form:

$$A = \begin{bmatrix} i_1 & i_2 & i_3 \\ j_1 & j_2 & j_3 \\ k_1 & k_2 & k_3 \end{bmatrix}$$

The matrix A is called attitude matrix or Direction Cosine Matrix (DCM) and represents the rotation from the inertial frame of reference to the body-fixed frame of reference. Defining this matrix is really important since it is characterized by the following useful properties [22]:

- The direction cosine matrix is a proper real orthogonal matrix so its transpose is equal to the inverse matrix:

$$A^{-1} = A^T \tag{2.1}$$

- The direction cosine matrix representing successive rotations is equal to the multiplication between the attitude matrices relative to the single rotations:

$$A'' = A'A \tag{2.2}$$

- The matrix A maps any generic vector from the inertial frame of reference onto the body-fixed frame of reference. Given a generic vector $\hat{v_I}$ in the inertial reference system, we have:

$$A\hat{v_I} = \begin{bmatrix} i_1 & i_2 & i_3 \\ j_1 & j_2 & j_3 \\ k_1 & k_2 & k_3 \end{bmatrix} \begin{bmatrix} v_1 \\ v_2 \\ v_3 \end{bmatrix} = \begin{bmatrix} v_i \\ v_j \\ v_k \end{bmatrix} = \hat{v_B} \tag{2.3}$$

  where $\hat{v_B}$ is the same vector written in terms of the body-fixed frame of reference.

  The direction cosine matrix doesn't have a univocal expression, it can be written in terms of different parameters according to what are the needs linked to the problem of attitude representation.

Two classical and very important attitude parameterization are described in the following sections.

2.3.1 Euler Angles representation

The attitude representation in terms of Euler angles is the most classic and is used because it's easy and immediate to understand its geometrical and physical meaning. The concept behind this parameterization is that we can go from a 1st frame of reference to a 2nd frame of reference performing 3 distinct right-hand positive rotations, where the angles characterizing those rotation are exactly the Euler angles. The sequence of rotation is not univocal but can be chosen arbitrary. In this work, a 3-2-1 rotation is considered and it's performed with the following steps [3]:

1) Rotation around the z-axis of the inertial reference system, represented by $\hat{c_3}$. The relative Euler angle ϕ is defined ***roll angle***.

2) Rotation around the y-axis of the intermediate frame of reference, denoted as $\hat{c_2}'$. The relative Euler angle θ is defined ***pitch angle***.

3) Rotation around the x-axis of the body-fixed reference frame, represented by $\hat{i}$. The relative Euler angle ψ is defined ***yaw angle***.

As said before, each rotation is described by its own direction cosine matrix but, thanks to the property given in (2.2), we can easily calculate the total attitude matrix. The full matrix A is given by:

$$A_{321} = \begin{bmatrix} c\phi c\theta & s\phi s\theta & -s\theta \\ s\theta s\psi c\phi - s\phi c\psi & c\psi c\phi + s\theta s\psi s\phi & s\psi c\theta \\ s\psi s\phi + s\theta c\psi c\phi & s\theta c\psi s\phi - s\psi c\phi & c\psi c\theta \end{bmatrix} \tag{2.4}$$

where $s = sin$ and $c = cos$.

If we know the matrix A, we can easily calculate the angle θ from:

$$sin\theta = -A_{1,3} \tag{2.5}$$

and once we get θ, we can find ϕ and ψ exploiting the other relations. This is always possible, except for the case in which θ is an odd multiple of 90° since, in that case, we can only know the sum of the other 2 angles, not their exact values [22].

Due to this singularities problem, different parameterizations of the attitude matrix are sometimes used.

2.3.2 Quaternions representation

The quaternions representation is particularly useful because, describing the attitude through it, we can avoid singularities in our model. However, with this parameterization we lose the immediate physical meaning of the values we're dealing with and we increase the computational effort. Quaternions are defined as:

$$q_1 = e_1 sin\frac{\Phi}{2} \tag{2.6}$$

$$q_2 = e_2 sin\frac{\Phi}{2} \tag{2.7}$$

$$q_3 = e_3 sin\frac{\Phi}{2} \tag{2.8}$$

$$q_4 = cos\frac{\Phi}{2} \tag{2.9}$$

Where $\hat{e}$ and Φ are defined, respectively, Euler axis and Euler angle, and represent the instantaneous rotation axis and the relative rotation angle. From their definition, we can see that the first three components represent a physical vector and that $|\bar{q}| = 1$, where $\bar{q} = (q_1, q_2, q_3, q_4)'$.

Applying those parameters for the attitude representation, the direction cosine matrix assumes the following form:

$$A(\bar{q}) = \begin{bmatrix} q_1^2 - q_2^2 - q_3^2 + q_4^2 & 2(q_1q_2 + q_3q_4) & 2(q_1q_3 - q_2q_4) \\ 2(q_1q_2 - q_3q_4) & -q_1^2 + q_2^2 - q_3^2 + q_4^2 & 2(q_2q_3 + q_1q_4) \\ 2(q_1q_3 + q_2q_4) & 2(q_2q_3 - q_1q_4) & -q_1^2 - q_2^2 + q_3^2 + q_4^2 \end{bmatrix} \tag{2.10}$$

Once we know A, we can get each quaternion component applying the following expressions:

$$q_4 = \pm\frac{1}{2}[tr(A) + 1]^{\frac{1}{2}} \tag{2.11}$$

$$q_1 = \frac{A_{2,3} - A_{3,2}}{4q_4} \tag{2.12}$$

$$q_2 = \frac{A_{3,1} - A_{1,3}}{4q_4} \tag{2.13}$$

$$q_3 = \frac{A_{1,2} - A_{2,1}}{4q_4} \tag{2.14}$$

So, what we basically do is find the 4th component of the quaternion and then write the other 3 in terms of it. Anyway, this is not the only way to compute the 4 components starting from the direction cosine matrix. We have, in fact, 4 possible combinations, where, each different combination, uses a different reference component of the quaternion. This particular elasticity of the quaternion representation is very useful in order to avoid singularities and increase the numerical computation [22].

As a final summary, the Euler angles representation is very useful for a good understanding of the physical meaning of the parameters but it can lead to singularities in our computation. The quaternion representation, instead, is good for its elasticity in the calculation of the different components, making us able to avoid singularities. Cons of this parameterization are the higher computational effort and the lack of an immediately understandable physical meaning.

2.4 Attitude kinematics

Since we are dealing with a moving body, it's clear that the relative position between the frames of reference is not fixed but changes in time and so does, consequently, the attitude matrix. Attitude kinematics is based on the computation of the time derivative of the direction cosine matrix, taking into account the relative angular velocity. Clearly, different attitude representations will also have different attitude kinematics representations.

In case of a representation in terms of Euler angles, attitude kinematics is addressed composing the angular velocities relative to the single rotations. Considering again the rotation 3-2-1 described in section 2.3.1, the total angular velocity is given by [3]:

$$\omega = \dot{\phi}\hat{c_3} + \dot{\theta}\hat{c_2'} + \dot{\psi}\hat{i} \tag{2.15}$$

For problems concerning the attitude dynamics and control is clearly interesting and relevant the knowledge of the angular velocity of the body to be controlled, so the angular velocity written in the body-fixed frame of reference. To find it, we have to calculate the components of the vectorial equation (2.15) on the body-axis reference system:

$$\omega_i = \dot{\phi}\hat{c_3} \cdot \hat{i} + \dot{\theta}\hat{c_2'} \cdot \hat{i} + \dot{\psi}\hat{i} \cdot \hat{i} \tag{2.16}$$

$$\omega_j = \dot{\phi}\hat{c_3} \cdot \hat{j} + \dot{\theta}\hat{c_2'} \cdot \hat{j} + \dot{\psi}\hat{i} \cdot \hat{j} \tag{2.17}$$

$$\omega_k = \dot{\phi}\hat{c_3} \cdot \hat{k} + \dot{\theta}\hat{c_2'} \cdot \hat{k} + \dot{\psi}\hat{i} \cdot \hat{k} \tag{2.18}$$

that leads to:

$$\omega_i = \dot{\psi} - \dot{\phi} sin\theta \tag{2.19}$$

$$\omega_j = \dot{\theta} cos\psi + \dot{\phi} cos\theta sin\psi \tag{2.20}$$

$$\omega_k = \dot{\phi} cos\theta cos\psi - \dot{\theta} sin\psi \tag{2.21}$$

The problems, described before, affecting the Euler angle representation, are also affecting the attitude kinematics.

In terms of quaternions, the description of the attitude kinematics is given, in compact form, by:

$$\frac{dA}{dt} = \Omega' A \tag{2.22}$$

where:

$$\Omega' = \begin{bmatrix} 0 & \omega_k & -\omega_j \\ -\omega_k & 0 & \omega_i \\ \omega_j & -\omega_i & 0 \end{bmatrix} \tag{2.23}$$

We can see that Ω' coincides with the *skew symmetric matrix* of the body angular velocity (with sign changed):

$$\Omega' = -[\omega_b^{\times}] \tag{2.24}$$

For what concerns the quaternion itself, its time derivative is given by:

$$\frac{d\bar{q}}{dt} = \frac{1}{2}\Omega\bar{q} \tag{2.25}$$

Where, the matrix Ω has this shape:

$$\Omega = \begin{bmatrix} 0 & \omega_k & -\omega_j & \omega_i \\ -\omega_k & 0 & \omega_i & \omega_j \\ \omega_j & -\omega_i & 0 & \omega_k \\ -\omega_i & -\omega_j & -\omega_k & 0 \end{bmatrix} \tag{2.26}$$

In this work, the equation (2.25) will be applied in a different form, decomposing the vectorial part of the quaternion and the scalar component of the same [36]. Namely:

$$\frac{dq}{dt} = \frac{1}{2}\Omega' q + \frac{1}{2} q_4 \omega_b \tag{2.27}$$

$$\frac{dq_4}{dt} = -\frac{1}{2}\omega_b^T \vec{q} \tag{2.28}$$

with:

$$q = \begin{bmatrix} q_1 \\ q_2 \\ q_3 \end{bmatrix} \; ; \; \omega_b = \begin{bmatrix} \omega_i \\ \omega_j \\ \omega_k \end{bmatrix} \tag{2.29}$$

2.5 Rigid body attitude dynamics

The fundamental equations governing the attitude dynamics of a rigid body are the so called Euler equations, given, in vectorial form, by:

$$\vec{M} = \dot{\vec{L}} \tag{2.30}$$

where $\vec{M}$ represents the resulting of external moments acting on the body and $\vec{L} = I\vec{\omega}$ represents the angular momentum of the body with respect the center of mass. From now on, talking about angular velocity, it will be always referred to the body angular velocity and it will be indicated simply by $\vec{\omega}$, omitting the pedix b.

In the most general case, both the angular velocity and the inertia matrix are time varying so, solving equation (2.30) for the angular acceleration $\dot{\vec{\omega}}$, we get the following expression:

$$I\dot{\vec{\omega}} = -\dot{I}\vec{\omega} + (\vec{M} - \vec{\omega} \times I\vec{\omega}) \tag{2.31}$$

which, in the case of constant inertia matrix simplifies to:

$$\dot{\vec{\omega}} = I^{-1}(\vec{M} - \vec{\omega} \times I\vec{\omega}) \tag{2.32}$$

A further simplification of the equation can be performed placing the body-frame in correspondence of the principal axis of inertia, since in that particular frame the inertia matrix assumes this shape:

$$I = \begin{bmatrix} I_x & 0 & 0 \\ 0 & I_y & 0 \\ 0 & 0 & I_z \end{bmatrix} \tag{2.33}$$

So, substituting (2.33) into (2.32), we get:

$$\dot{\omega_x} = I_x^{-1}[M_x + (I_y - I_z)\omega_y\omega_z] \tag{2.34}$$

$$\dot{\omega_y} = I_y^{-1}[M_y + (I_z - I_x)\omega_z\omega_x] \tag{2.35}$$

$$\dot{\omega_z} = I_z^{-1}[M_z + (I_x - I_y)\omega_x\omega_y] \tag{2.36}$$

where the x-component lies along $\hat{i}$, the y-component along $\hat{j}$ and the z-component along $\hat{k}$. In this work, as specified in section (2.2), the body-fixed reference frame is assumed to be coincident with principal axis of inertia so the last simplification described is applied.

In general, the term $\vec{M}$ appearing in Euler's equations, can be decomposed in 2 different components: external torques (or disturbance torques), M_{ext}, and control torques, M_c. In the prototype developed, control torques are given by:

- *Reaction Control System (RCS)*
  Control torques are given by 8 cold-gas thrusters and each Euler angle can be modified and controlled.

- *Thrust Vector Control (TVC)*
  Control torques are given by the angular displacement of the engine that creates an off-set between the center of mass and the direction of thrust vector. With this system we can only control *pitch* and *roll* angle.

These subsystems will be described in details in chapter 3.

For inputs on the disturbance torques that can affect the vehicle, these may include but not be limited to: torques given by interaction with the atmosphere and by wind gusts, disturbance due to the sloshing of the fuel inside tanks,etc. Sloshing is a phenomenon that occurs in any vehicle experiencing accelerated motion, it is due to the interaction between the fuel and the surface of the tank and can be particularly strong in case of partially filled tanks [28]. This phenomenon is really hard to assess both for its particular dynamics and for the fact that the volume of liquid in tanks is continuously changing in time. In addition, in presence of TVC system, when the mass of the engine is not negligible with respect the total mass, also the relative motion of the engine with respect the body is source of disturbance torques. All of these sources of disturbances should be taken into account in order to avoid instability problems.

2.6 Thrust vector control: literature review

Thrust vectoring is defined as the capability of an aircraft or spacecraft to modify the position of an engine and point the thrust vector in any direction, in order to control the attitude and the angular velocity [31]. This concept has been widely used in many different applications, going from fighter jets to small spacecrafts, and for different purposes. The deflection of the thrust vector is usually obtained by means of different strategies, relative to the type of propulsion system on which the TVC is applied. In general, thrust vectoring methods can be grouped in 3 different categories:

1) Reactive fluid injection
2) Exhaust flow deflection
3) Engine mechanical manipulation

2.6.1 Reactive fluid injection

This method of thrust vectoring is generally applied on rocket engines and consists in injecting a fluid into the side of the flow exiting from a nozzle, by means of particular injectors mounted on the sides of the engine. When the reactive fluid is injected in only one side of the exhaust gas, it changes the properties of the flow, resulting in a different thrust value on that side. This method also increases the axial value of the thrust because of the higher pressure, due to shock waves, and the added mass and energy to the flow. Usually, in order to increase the effect of this system, denser reactive fluid are preferred [14]. An example of the application of

this system is the TitanIIIE-Centaur rocket launcher by NASA [1]. Below a scheme of the flow injector on the launcher:

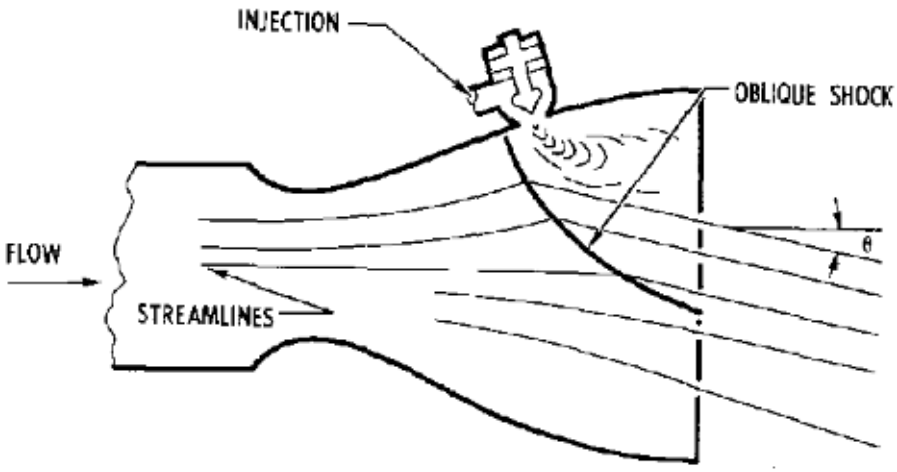

Figure 2.3: Reactive flow injection on TitanIIIE-Centaur (NASA) [1]

2.6.2 Exhaust flow deflection

The method of exhaust flow deflection consists in placing particular surfaces at the exit of the nozzle that can be oriented in order to direct the flow, and consequently the thrust vector, into the desired direction. The most common of those surfaces are external jet vanes and external additional nozzles. This method of thrust vectoring is used both for rocket and jet engines. Jet vanes are external paddles that are placed at the exit of the engine and that can be driven into different configurations in order to guide the exhaust gas. Their main pro is that with them is possible to control each rotation angle, roll included, with just one single engine, not possible for gimbaled engines. A con is that their very presence degrades and reduces the rocket's efficiency. Vanes are, in general, either designed to be resistant to very high temperature or are constantly cooled down, in order to prevent them from melting. However, lately, some particular composites vanes have been designed to withstand the pressure and temperature of the exhaust flow in the very first part of the flight, until the speed of the body is enough to use normal control surface like aerodynamic fins. Once the control passes to fins, vanes rapidly degrade and dissolve. Those particular vanes are known as dissolvable vanes [11] and are very useful when a lower mass is needed.

A famous example of the application of external vanes are the V-2 rockets, developed during the World War II.

Another solution to obtain the thrust vector tilting by deflecting exhaust gases is the application of an additional external nozzle that is mounted at the exit of the engine. In this way, the desired effect can be obtained by moving the second nozzle while the main engine is kept still.

This category is distinguished from the mechanical manipulation group since, in this particular case, the thrust vectoring is accomplished by the deflection of external components, without moving any part of the engine.

2.6.3 Engine mechanical manipulation

Vehicles exploiting this particular systems are equipped with movable engines or shape-changing nozzle that can be oriented and/or modified to reach the desired goal. By tilting the engine or the nozzle, an off-set between the thrust vector and the center of mass will be generated, giving rise to control torques around the center of mass itself. Those particular systems are usually also referred as gimbaled thrust systems and the angular displacement of the engine is defined gimbal angle. The maximum gimbal angle reachable through the TVC systems defines a cone in which the engine can move, called cone of operation.

Figure 2.4 shows an example of a gimbaled thruster.

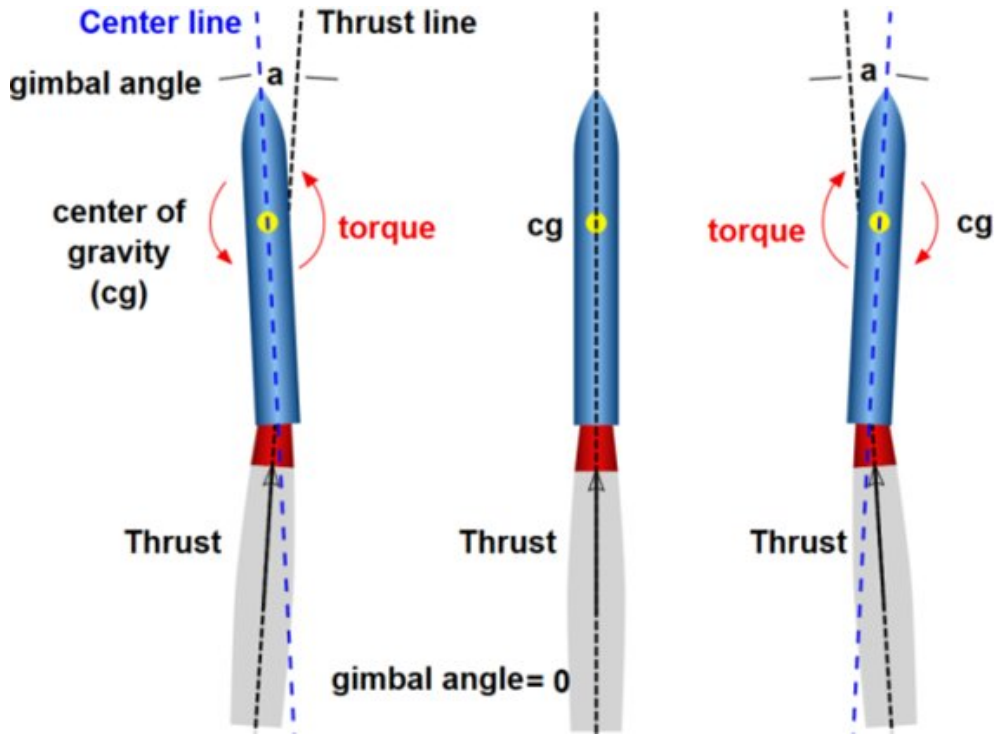

Figure 2.4: Example of gimbaled thrust on a rocket [6]

TVC through mechanical manipulation of an engine is widely used, not only on

rockets but also on aircrafts and spacecrafts. In the first two categories described, thrust vectoring was reached by acting directly on the exhaust flow exiting from the nozzle. In the last case, the flow goes through the nozzle without any modification since the actuation to get the desired deflection is given directly on the engine. When the vehicle is equipped with a single motor, thrust vectoring allows the control only of pitch and yaw angles and has no effect on roll motion (defined as the angular motion around the axial direction of the vehicle). The only way to have a full control on the rotational dynamics of the system through mechanical manipulation is to combine the thrust vectoring in, at least, 2 different engines.

The typical method used to have TVC on jet engines is the usage of adjustable nozzles that can modify their shape in order to assume a deflected configuration, changing so the thrust direction.

In rocket engines, instead, the actuation of the nozzle is usually obtained through the displacement of linear actuators that makes the engine move around a particular joint that fix it to the whole structure. Different types of joint are illustrated below:

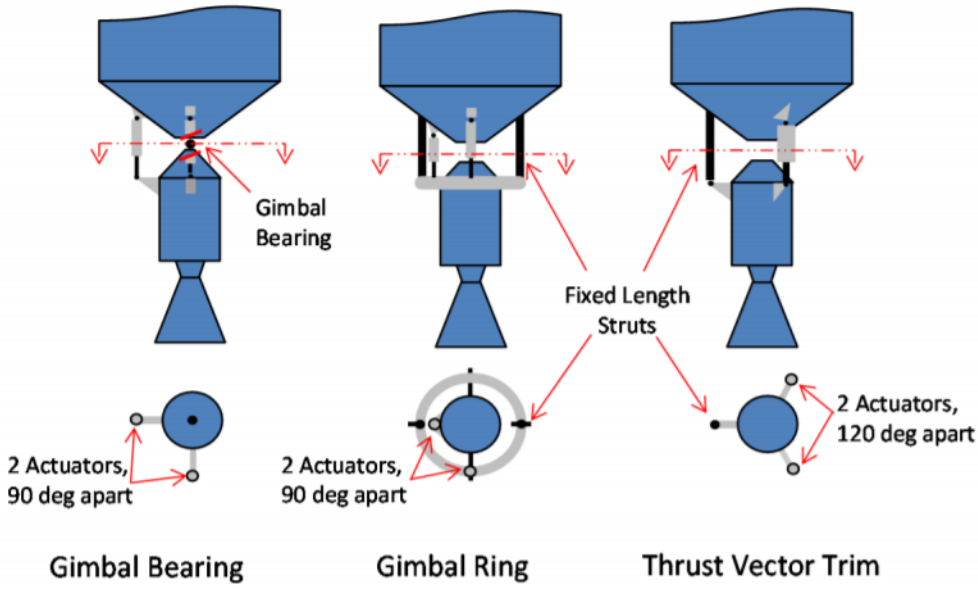

Figure 2.5: Typical joints used on gimbaled engines [10]

The gimbal bearing is a joint that allows 2 degrees of motion and that can carry most of the thrust load. The engine is driven by two actuators connected to it, mounted 90° apart to provide a full two-axis movement. The gimbal bearing can be replaced by a gimbal ring that allows the same two-axis motion. In case of the usage of a single ring, the actuators will always be mounted 90° apart but, in this case, one of them will be attached to the engine and the other one to the ring. We have to underline that 2 actuators are the minimum number to have a full motion

of the engine but usually more than 2 is used for redundancy. The last joint showed in Figure 2.5 is quite different from the others since, in this case, the connection between the engine and the structure is given by a lateral ball and socket joint and the motion is driven by 2 actuators mounted 120° apart. This configuration was considered during the Nuclear Engine for Rocket Vehicle Applications (NERVA) program [10]. The main advantage of this configuration is that gimbal bearing and gimbal ring can be avoided. However, the con is that the thrust load must be carried by the lateral connection and by the actuators, making this joint more suitable for low-thrust applications.

Thrust vectoring is commonly used also in spacecrafts and landers. For example, Apollo lunar modules were equipped with a gimbaled engine in order to keep the thrust vector aligned with the center of mass during the gravity turn maneuver in the braking phase of lunar descent [32]. For spacecraft applications, TVC is not always applied on the main propulsion system but also on the thrusters used for attitude control. In [9] is illustrated a spacecraft detumbling procedure using, together with momentum wheels, a reaction control system based on gimbaled thrusters that can adjust their position to get the optimal control torque.

Recalling the LLRV, that vehicle was also equipped with a gimbaled engine but in that case the joint was only used as a gyroscope joint to give an offset between the chassis and the engine, in order to keep the latter always vertical. The aim of this solution was to cancel out 5/6 of Earth gravity acceleration in order to simulate a Moon environment [20].

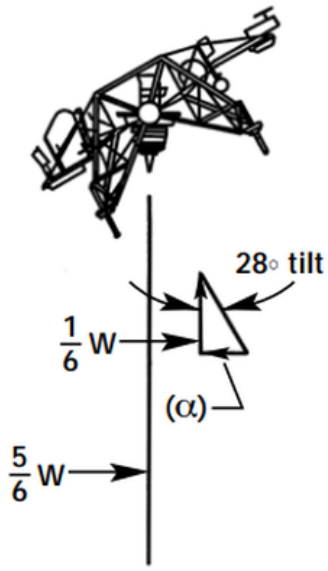

Figure 2.6: LLRV gimbaled engine [20]

As we see, Thrust Vector Control is applied for different purposes and by means of different configurations and systems. Generation 2 of LEAPFROG is the first one equipped with this technology so an accurate research had been carried out to find the best way to apply TVC on this kind of vehicle. Many of the concepts described before had been analyzed and considered in order to find the best solution that can match with the characteristics of the current prototype and with the ideas planned to be applied in next generations.

Chapter 3

Preliminary hardware design

In this chapter are presented and described the considerations and choices made during the design phase of the hardware composing the new prototype, with a particular focus on the hardware dedicated to the TVC system. All the choices have been taken according to the requirements fixed for this project.

3.1 Project budget and requirements

Since a new generation of the project started in September 2019, an entire new prototype had to be designed and developed from scratch, trying to meet as much as possible the initial requirements and goals, stated in chapter 1. The first objectives taken into account were the increase of the payload capacity, the improvement of control and guidance subsystems and the self-reconfiguration capability that the prototype should have. All of this without moving to much from the concept of being a low cost risk reduction platform for simulated lunar flight and landing.

In the following sections the different components of the prototype are described according to the decisions made during the design process.

3.2 Structure

The first phase of the design work was focused on the realization of a new structure that could allow an increase off carriable mass, looking forward to a future possible payload application, and an increase in structural resistance. The previous generations, as also shown in figure 1.2, were characterized by a single platform with a 4-leg configuration, a central jet engine and a set of cold-gas thrusters for attitude control. The platform was mainly used just as a storage bed for all the subsystems equipped on the two prototypes while all the load of an eventual free fall would have

been carried by the legs only. The idea to improve the structure of the new vehicle was to realize a double-layer configuration where two distinct platforms, similar to the ones used in previous prototypes, are connected through an internal chassis. The full CAD design proposed for the new structure is shown below:

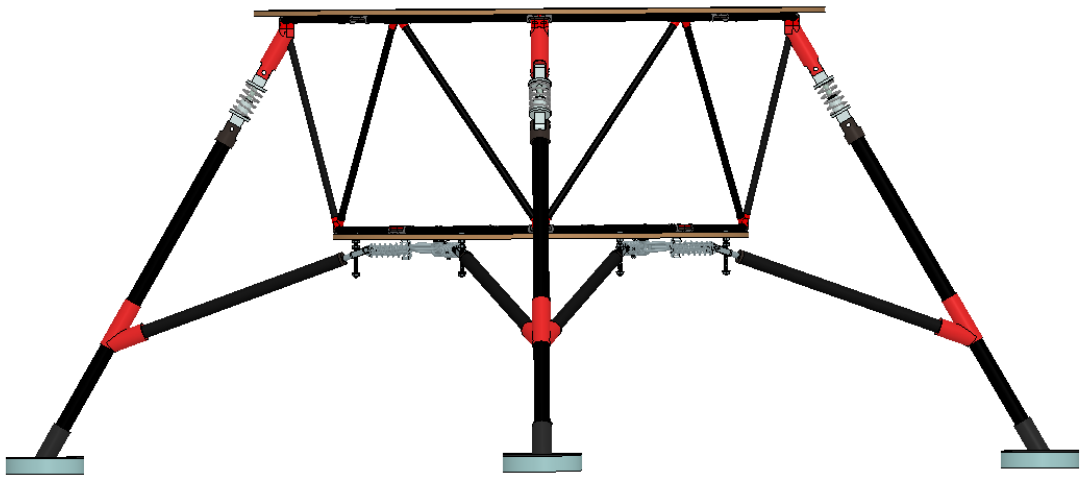

Figure 3.1: Structure of Generation 2 - CAD model (front view)

The total height of the structure is 86.6 cm while the total width is about 178 cm. The 4 leg configuration has been applied also in this new prototype.

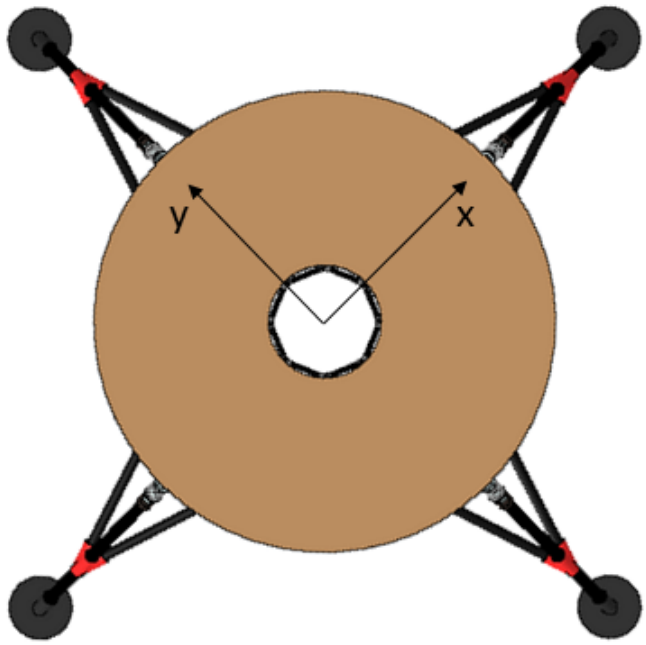

Figure 3.2: Structure of Generation 2 - CAD model (top view)

The two axis in figure 3.2 represent the direction of principal axis of inertia.

The reason for the choice of this particular configuration is that the double layer increases the storage capability, giving the chance to place on board all the subsystems needed, saving also some space that could be used for an eventual extra payload to test on the vehicle. Moreover, the internal chassis can withstand loads due to a possible free fall, reducing the effort of the legs. Thanks to the usage of carbon fiber, the total mass of the structure is around 8 Kg.

Structural analysis and simulations of the entire model had been performed by other team members in parallel with the design work. The different parts composing the overall structure (chassis, legs and platforms) are described in detail below.

3.2.1 Chassis

The chassis is a reticular structure characterized by two layers connected by transversal rods. In order to have a light weight and a high resistance as well, all the tubes used are standard modulus carbon fiber tubes, ideal for bending applications. The rods are connected each other with particular connectors (Dragonplate connectors) designed exactly for this material. Some additional connectors will be 3-D printed in Acrylonitrile Butadiene Styrene (ABS), to match with LEAPFROG's particular geometry.

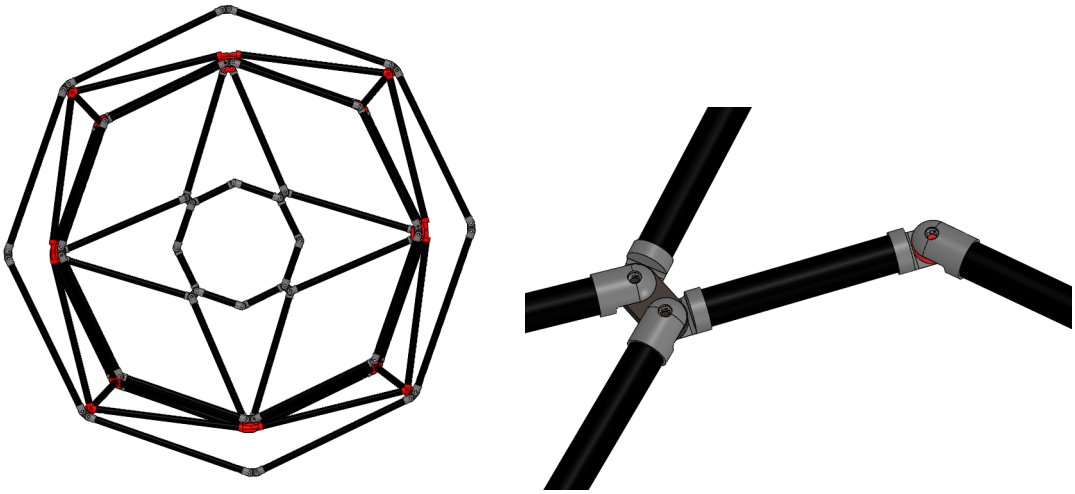

(a) Full chassis (top view) (b) Particular of connections between rods

Figure 3.3: Carbon fiber chassis - final version

The red parts visible in figure 3.3 represents the components that are designed to be 3-D printed. The chosen octagonal shape of the chassis is due to manufacturing and high costs issues. The initial designed considered a circular shape to match with

the geometry of the platforms but that particular solution would have been difficult to realize in labs and too much expensive for a realization in external companies. For this reason, the final choice went to the usage of simple rods connected such to result in a shape as close as possible to the circular one, keeping the overall cost contained.

3.2.2 Legs

The 4 legs are realized with tubes of the same material used for the chassis and each of them is characterized by a main rod connecting the foot to the upper layer of the structure, and two support rods that connect the leg with the lower layer. This particular geometry was chosen to distribute evenly the load among the chassis,avoiding a full concentration in a single point. Furthermore, the particular inclination of the legs was chosen for stability reason but also for possible issues that could be encountered due to the presence of the engine. The engine, in fact, is placed in correspondence of the lower layer of the chassis and the high temperature of the exhaust gases could affect the carbon fiber. An high inclination keeps the legs as far as possible from the engine.

Besides the material used, in order to reduce and dissipate the stress affecting the structure, connection between the leg and the upper part of the chassis comes through a shock absorber while the mounting on the lower layer is made through spring connectors that can displace in presence of a load and then come back to the original position. The 4 feet are realized in memory foam material to further reduce the stress affecting the structure. The connector used to attach the support rods to the main rod will be 3-D printed in ABS material as well.

3.2.3 Platforms

The two platforms connected on the upper and lower layer of the chassis are the storage area for embedded electronics and other subsystems equipped on the prototype.

Both of them are characterized by a circular shape and a circular hole in the middle. The reasons of the holes are that the lower disc will have the engine going through it while the hole on the upper one ensures that enough air comes to the engine itself. The material used for the realization of the platforms is a Divinycell foam board material stiffened with an epoxy and fiberglass lamination, same procedure used for the realization of the platforms mounted on previous prototypes [37]. The choice for this material is due to its high strength to weight ratio The attachment to the chassis is performed through particular rounded mounting brackets.

3.3 Propulsion system

For the propulsion system, the final choice went to adopt a kerosene powered jet engine by JetCat company, the same type of engine used for generation 0 prototype. The reason is that those engines are easy to manage and doesn't provide an excessive unwanted yaw rotation due to rotating blade, as a propeller may cause. The problem of the undesired rotation could be eliminated with the installation of a rocket engine, thing planned for future generations.

The generation 0 prototype had installed a JetCat P100 for a much smaller vehicle so, considering that the structure by itself has a mass around 12 kg, the new engine adopted is a JetCat P300 PRO that can provide $200N$ of thrust more than the previous one. This engine upgrade is necessary since we need a sufficient thrust to carry the structure, all the subsystems installed on it and an eventual payload to test on the prototype, even if the cost of the P300 is quite higher than the P100 one.

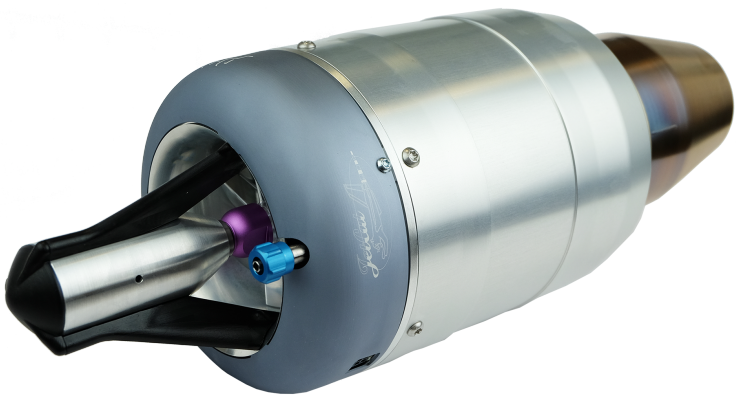

Figure 3.4: JetCat P300 PRO [2]

The engine is characterized by a single compressor stage, a combustion chamber and a single turbine stage, and comes with its own telemetry and an embedded Electronic Control Unit (ECU), so they don't have to be realized from scratch saving time in development. The ECU manages fuel pumps, valves and electronic system thanks to a feedback closed loop that provides back to the engine itself information about RPM of the blades and temperature of exhaust gases. Integrated to the engine there's also an electric starter used for the initial firing. Other important components of the engine kit are the clamps that are designed and customized exactly for the attachment of the engine to the host structure. The propellant used to feed the engine is store in a dedicated tank placed above the upper platform of the vehicle.

The principal technical specifications of the engine are listed in the following table:

Table 3.1: JetCat P300 PRO technical specifications [2]

Basic technical specifications	Values
Max RPM	106000
Idle RPM	35000
Thrust at max RPM (N)	300
Thrust at idle RPM (N)	14
Exhaust Gas Temperature (EGT) range ($°C$)	480 - 750
Mass flow (kg/s)	0,5
Exhaust gas velocity (km/h)	2160
Fuel consumption at idle (kg/min)	0,143
Fuel consumption at maxRpm (kg/min)	0,784
Weight (kg)	2,73
Diameter (mm)	132
Lenght (mm) including starter	380,5

The term idle used in the table refers to the minimum operating condition.

3.4 Reaction control system

The reaction control system is one of the two attitude control subsystems equipped on LEAPFROG. It is composed by 8 thrusters distributed along the circumference of the upper platform, with the disposition shown in figure:

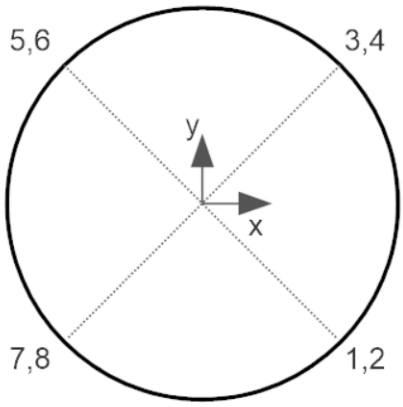

Figure 3.5: RCS thrusters placement

The two axis depicted in figure 3.5 represent the two in-plane principal axis of inertia (the z axis is perpendicular and coming out the plane). The eight thrusters are placed such that 4 of them (number 2,4,6,8) are used for yaw control and the other 4 (number 1,3,5,7) for roll/pitch control. The reason of the 45° offset between the thrusters position and the principal axis of inertia is due to the fact that the latter, as shown in picture 3.2, run through the legs of the prototype and placing RCS thrusters above them will result in disturbances due to the interaction between the cold-gas and the legs themselves. Clearly, not having thrusters aligned with principal axis of inertia, we cannot control the rotation angles with a single thruster but we need a combined action of two of them. In particular, the firing logic is the following:

- positive yawing moment → 2 and 6 firing
- negative yawing moment → 4 and 8 firing
- positive rolling moment → 1 and 3 firing
- negative rolling moment → 5 and 7 firing
- positive pitching moment → 1 and 3 firing
- negative pitching moment → 3 and 5 firing

The particular firing logic has been chosen to minimize lateral displacement during attitude control maneuvers. The thrusters are connected, through dedicated pipe lines, to a total of 4 tanks (1 tank for each pair of thrusters) filled with 4000 psi compressed air. The pressure of the air coming out from the tank is tuned by a pressure regulator (one for each pipe line) according to the needs. The air flow coming out from each thruster, instead, is regulated by solenoid valves which open and close according to the signal coming from an in-board CPU receiving data from an Inertial Measurement Unit (IMU) that provides information on the current attitude of the vehicle. The solenoid valves are constituted by an inner coil and a ferromagnetic plug tied, through a spring, into the flow channel, closing it. When the electric signal is sent to the valve, a current starts flowing into the coil and generates a magnetic field that attracts the ferromagnetic plug, opening the channel. Once the electric signal, thanks to the spring, the plug comes back to its standard position, closing the channel again. Those solenoid valves are very useful for this kind of application since their response is pretty fast, opening and closing the channel almost immediately.

Below the block diagram of the Reaction control systems pipelines:

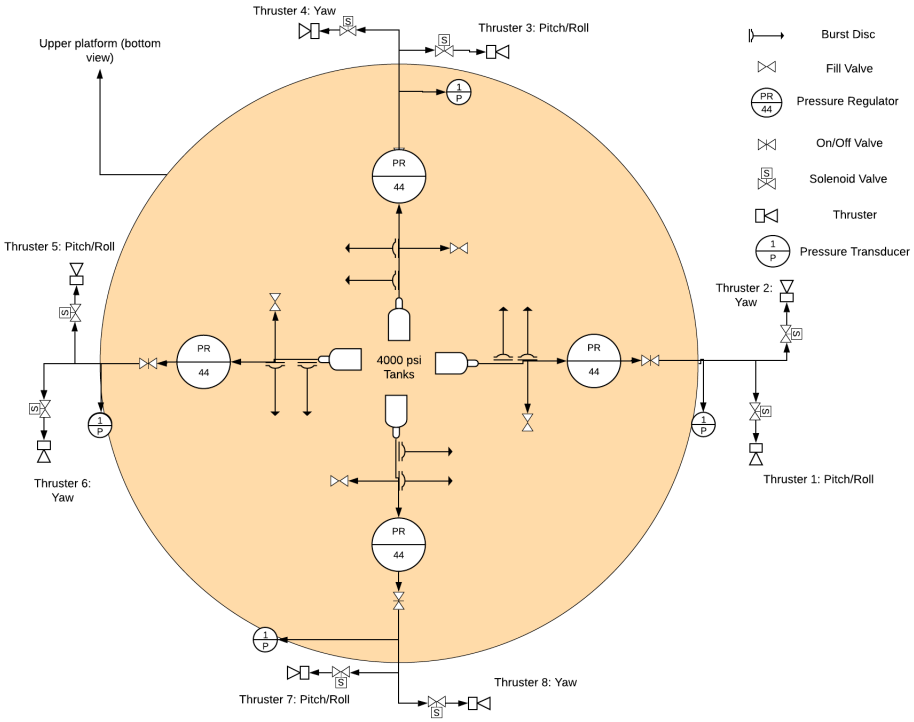

Figure 3.6: RCS block diagram

3.5 Thrust Vector Control system

The design of the thrust vectoring system has been the main focus of the presented work. This kind of control system is commonly used in lander spacecrafts mainly to keep the thrust vector parallel to the velocity of the spacecraft itself during landing maneuvers, in order to slow down and reach a final soft landing.

For its part, LEAPFROG is meant to be a re-configurable prototype capable to perform multiple tasks modifying the working configuration of its various subsystems. For the TVC, the guideline has been the design of a system that could be used both as a guidance and navigation system during flight phase and as an attitude control system during hover or landing phases. About those purposes, the design of the attitude control setting is the most delicate since, while guidance and navigation requires slow steering maneuvers and consequently slow changes in thrust vector direction, attitude control system has to equilibrate and balance the vehicle every time and it could be called to act against rapid and abrupt attitude variations due to any kind of external disturbance that can affect the dynamics of the system. Although the above described reaction control system, thanks to the fast response given by the solenoid valves, is capable to act rapidly against disturbances, exploiting the thrust

force can reduce the expenditure of energy and cold-gas mass. The main challenge, so, has been the design of a system that could respond to attitude changes as fast as possible, trying to reduce the usage of reaction thrusters. To achieve this goal, since the response of the TVC system, clearly, cannot be infinitely fast, some constraints and boundary conditions about the range of action had to be fixed, letting the TVC work within some predefined values of thrust deflection angle and adjusting the attitude with the RCS when the eventual required deflection angle exceeds the limits imposed. It is then clear that the synchronization between the two different attitude control system becomes a crucial point for the overall control logic of the prototype. This synchronization, in terms of hardware, is achieved with a merged system of three different CPU's composed by a main general control unit and two control units dedicated respectively to the RCS and TVC systems, that can work separately and also communicate between each other (a more detailed description about the electronics will be given later on).

The first point to assess was how we could obtain thrust vectoring in our system, considering all the different technologies available in literature. As underlined in section 3.3, the engine chosen for the prototype is an axial jet engine, designed with particular characteristics that cannot be modified or are hard to. For this reason, a solution considering the injection of a secondary fluid was immediately discarded since it would require the modification of the nozzle in order to place injectors around it, proceeding that can be hard and delicate. Moreover, this kind of application requires a precise quantification of the effect of the secondary flow on the main flow, making the deflection of thrust vector hard to assess. The main two options, then, were the deflection of exhaust gases and the mechanical manipulation of the engine. This type of jet engines are characterized by a rigid full body where the nozzle is directly connected with housing for the turbine, the compressor and the combustion chamber. This means that a relative motion of the nozzle with respect the main body of the engine is impossible. This is the main reason for which, on jet engines, is usually applied a deflection of exhaust gases method [25]. Furthermore, those engines are usually applied in light vehicles and the system used to achieve the thrust vectoring should not add an excessive extra mass. As discussed in section 2.6.2 the deflection of the gases coming out from the nozzle is typically achieved using external vanes or an external additional nozzle, systems that are independent from the engine and that allow to keep the latter always fixed to the structure. However, even these applications have some intrinsic complications to deal with during the design process.

Those can be summarized as follow:

1) *Material-related issues*: Those systems (vanes and external nozzle) are directly

in contact with the exhaust gases that, as shown in table 3.1, can reach a temperature around 700 °C so the material should be high-temperature resistant, aspect that could lead to an expensive choice.

2) *Engine performance variation*: When a system is acting at the exit of an engine nozzle, it unavoidably affects and changes the specifications and performance of the engine itself. For example, the presence of external components reduces the velocity of the exhaust flow and consequently the thrust provided by the engine, being the two quantity directly proportional, as underlined by the thrust equation [26]:

$$F = \dot{m}_e u_e + (P_a - P_e)A_e \tag{3.1}$$

where F represents the thrust vector and u_e the velocity of the flow in the direction of vehicle's motion. The adoption of those systems necessarily requires a deep testing phase where the variations of the engine specifications must be quantified and addressed.

For this reasons, combined to the fact that we can allow a little increase of the vehicle mass, the final decision went to reach thrust vectoring by mechanical manipulation of the engine. Moreover, applying this concept, the same control logic used to drive the thrust vector in this prototype can be re-used in next generations also in case of the installation of a mono-propellant rocket engine as propulsion system.

Since, as stated before, in JetCat P300 the nozzle is fixed to the main body, the thrust vectoring can be reached only through mechanical manipulation of the entire engine. Concerning this, a simple gimbal joint cannot be used with this type of engine since the upper part must be free to allow the air to enter the compressor, so, the final idea to get the adjustability of thrust vector direction was to gimbal the engine through a gimbal ring.

A gimbal ring is a gyroscopic joint composed by a set of concentric rings that can rotate with respect each other, along different directions. This particular joint, when connected around a body, allows the body itself to tilt in any wanted direction.

In our particular application, the final design of the gimbal ring provides three concentric rings where the inner one is directly connected to the engine and the outer one is attached to the chassis. The connection between the inner ring and the engine is obtained through particular clamps that are custom designed exactly for this engine and provided by the same company. Thanks to the three ring configuration we get one degree of freedom with the relative rotation of the inner ring with respect the middle ring and another degree of freedom with the relative rotation of the

middle ring with respect the outer one. The rotations are allowed by the presence of particular pins that interconnect the ring and that, at the same time, have the role of axis of rotation.

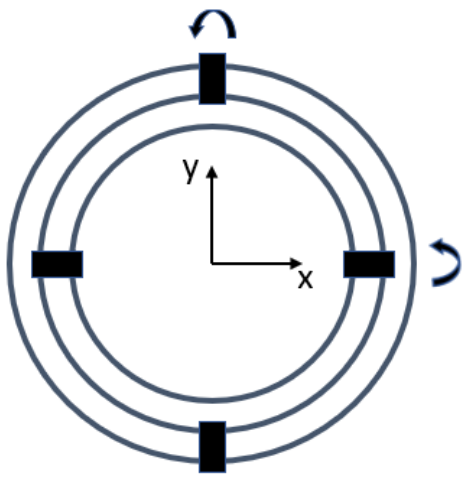

Figure 3.7: Conceptual sketch of the gimbal ring

As we can see from figure 3.7, the gimbal's axis of rotation are perfectly aligned with the principal axis of inertia of the vehicle (x and y in the figure). The choice is related to a simpler actuation procedure since, in case of pure pitch or pure roll motion, we can provide the control torque by rotating only one of the rings so, as will be described later on, activating only one linear actuator.

Once decided the method to use to obtain the TVC, the second phase of the work regarded the mechanical design of the gimbal ring.

3.5.1 Gimbal joint design

Gimbal rings are very particular joints that are custom designed for the applications they're intended for. The particular geometry of the prototype, combined with the engine used, required a newly designed joint. The design of the gimbal ring had been driven by some requirements that can be summarized as follows:

- Overall component as light as possible, so not to add a too much extra mass to the vehicle
- Enough resistance in order to withstand the thrust given by the engine
- Use of COTS (Commercial Off The Shell) material, in order to keep the cost sufficiently low

- Not too complicated geometry in order to allow an in-lab machining and fabrication with the machinery available.

In order to meet the different requirements, the final choice for the material went to usage of 3 mm thick aluminum 6061-T6 sheets. This particular material is widely used, also in aerospace applications, for its good machinability, medium to high strength and light weight, all of that at an affordable price [24]. The only components of the gimbal ring with a different material are the inter-connecting pins since they're carrying both the weight of the rings and both the thrust of the engine. For this reason, the pins are characterized by a stainless steel screwed shaft where a couple of bushings are placed in order to facilitate the rotation. The distance between rings is kept through the usage of spacers. Bushings and spacers are made in stainless steel too. Concerning the geometry, the first and most intuitive idea was the realization of simple rounded shape rings to connect with pins. However, this geometry had some issues in terms of attachment to the structure and, primarily, in terms of manufacturing. A round shape, in fact, requires a very precise bending of the aluminum sheet, hard to achieve with the available machines. Moreover, just because the gimbal ring is made out from aluminum sheets, we could not get a full body ring. For this reason, the final decision went to build the gimbal joint by assembling together different aluminum plates, easy to realize with the available equipment. The final shape recalls the octagonal geometry of the lower layer of the chassis in order to get an easier attachments between the two parts. In addiction, the inner ring of the joint also hosts two vertical plates that run along the sides of the engine and that are used as a connection point for the actuators.

Final design of the gimbal ring mounted on the engine:

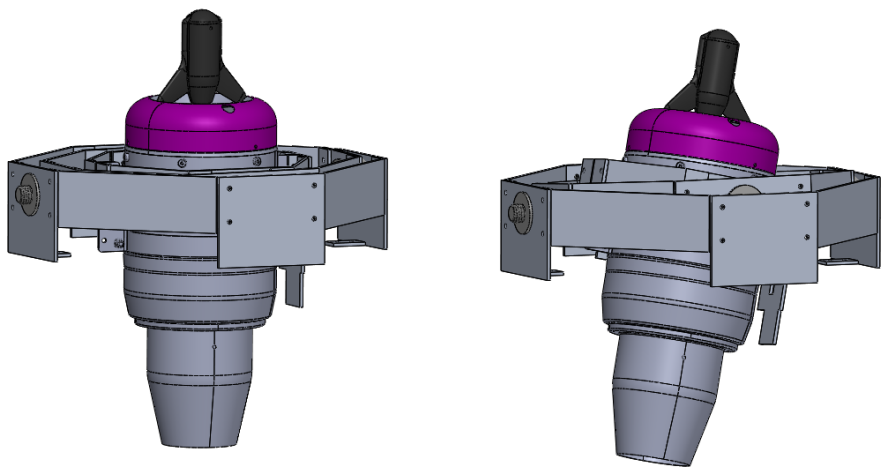

(a) Rest condition (b) Displaced condition

Figure 3.8: Gimbal ring mechanical design

3.5.2 Actuation system

As briefly mentioned before, while the gimbal ring allows the motion of the engine, the actual movement is obtained thanks to the action of two linear actuators that are placed 90° apart and that act at the same time on the engine. In particular, they are placed such to be aligned with principal axis of inertia of the prototype. In this way, a pure pitch or roll rotation is adjusted with the displacement of a single actuator.

The actuators employed, in order to save money, were not chosen from the market but, instead, they were some remaining actuators available at SERC from a different project. This aspect was challenging since, being those not properly designed for this system, they're work had to be optimized in order to get the best performance out of them.

Going into detail, they are industrial linear electro-mechanical actuators from Windynation company (Windynation LIN-ACT1-04). The sketch is given below:

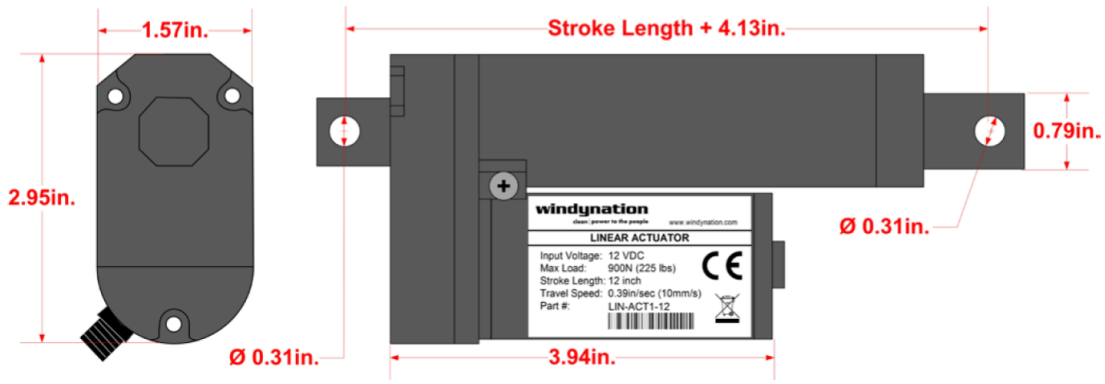

Figure 3.9: Windynation linear actuator [33]

The main technical specification are listed in the following table:

Table 3.2: Windynation LIN-ACT1-04 technical specifications [33]

Basic technical specifications	Values
Stroke Length	102 mm
Rated Load	900 N
Travel Speed (Max load)	10 mm/s
Rated Voltage	12 VDC
Current Draw (Max load)	$\leq 25A$
Operating Temperature	-26°C to 65°C
Duty Cycle	25%

Looking at table 3.2, between the different specifications, the most important for our application are the rated load, the travel speed, the stroke length and the duty cycle. All those parameters had to be taken into account because they strongly affect the performance of our control system. For example, the duty cycle parameter shows that actuators can only work for 25% of the time, with a 75% of non working condition. This shows that a full TVC-based control system is hard to have, even if attitude control, in particular situation, can also request just few seconds of action. The problem of the duty cycle could be avoided with the usage of hydraulic actuators. However, electro-mechanical actuators are usually preferred because they represent a lighter, safer and easier to maintain solution for this kind of work [8]. While duty cycle affects the working time of the actuators, the other parameters directly affect the performance of the latter, in particular the speed of actuation. Luckily, those actuators have not to carry a very high load since the engine has a weight of 2,73 kilograms and it is totally sustained by the gimbal ring. Actuators, so, only have to face the inertia of the engine itself. This means that their velocity is much higher than the one given in table 3.2. The manufacturing company provides the following graph showing the relationship between the carried load and the speed of actuation.

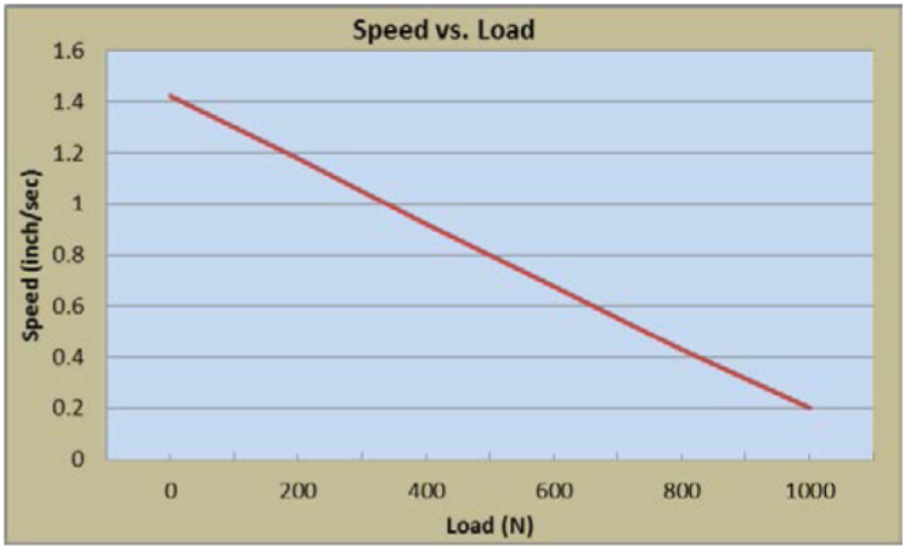

Figure 3.10: Actuators: speed vs load [33]

As we can see, in case of load-free movement, the speed of the actuators increase up to 35,6 mm/s (1,4 inches/s). Taking into account the same considerations made before about the weight of the engine, we can assume that the actuators work at a velocity close to the maximum one. Introducing a sort of "safety factor", in

the present work is assumed that the actuators work at a speed of 30 mm/s (1.18 inches/s). However, in future work, a test of the actuators on the engine fired should be performed in order to assess the real working speed. Actuator's performance can be further improved optimizing the placement of the actuator itself with respect the engine. Typical applications of the TVC on aircraft or rockets, because of the particular geometry of the engines, are characterized by an inclined position of the actuators driving the engine. However, this particular working condition is limiting the actuators performance for two main reason:

1) When the actuator is inclined with respect the gimbal joint, its displacement does not contribute entirely to the movement of the engine. In fact, only the component perpendicular to the joint is actually acting on the engine displacement while the parallel component is not useful for the purpose. The actuation speed is then reduced since a larger displacement is required to achieve a desired point.

2) Inclined actuators means that their pivot point is not perpendicular to the flying direction. This condition results in a strong coupling in the load motion between pitching and yawing directions, making more difficult the coordination between the two actuators [18].

In our application, actuators should be as fast as possible in order to have a good controllability of the attitude through the TVC. Taking into account what explained before, thanks to the particular position in which the engine is placed, the actuators, on LEAPFROG, are placed perfectly perpendicular to the axis of motion, such to have the full displacement of the same contributing to drive the engine in the desired position.

A further improvement is achieved minimizing as much as possible the distance between the gimbal point, i.e. the point around which the rotation of the engine occurs, and the point in which the single actuator acts on the engine itself. As already pointed out, the key behind the Thrust Vector Control is the creation of an offset between the center of mass of the vehicle and the direction of the thrust vector by inclining the engine. When we talk, then, about a fast actuation, what is meant is that we should be able to incline the engine as fast as possible. Reducing the distance between the center of rotation and the actuator acting point helps in this purpose since, for the same amount of linear displacement, with a shorter distance a bigger angular displacement of the engine is induced and so we increase the tilting speed.

The installation configuration of the actuators on LEAPFROG is depicted in figure 3.13.

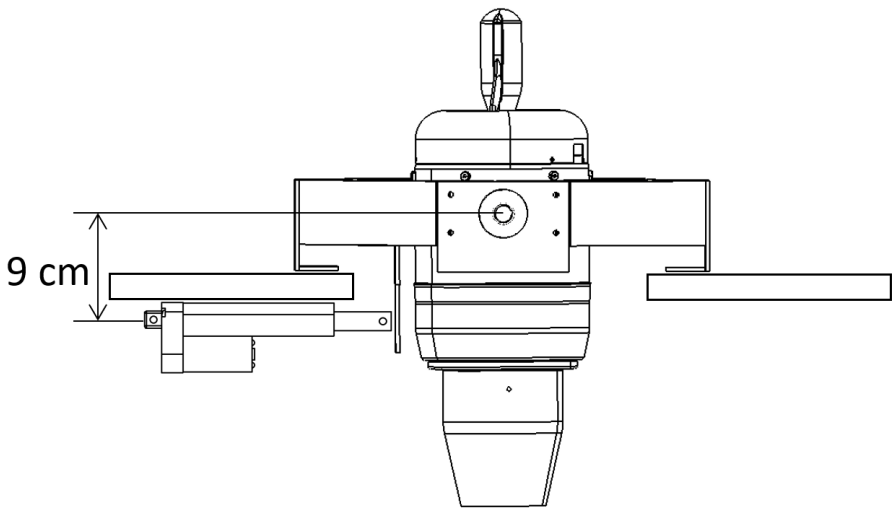

Figure 3.11: Actuators installation scheme

As shown in the picture, in our practical case the distance between the two point is about 9 cm. From this data, combined with the assumed actuators speed of 3 cm/s, we can see that the angular actuation speed of this system is around 0.3218 rad/s (about $18.4°/s$). However, even if the actuation speed is quite satisfying, the angular motion of the engine is limited by different factors like the interference with the chassis and the restricted movement of the actuators due to the presence of the platform. For this reason, a limited work range for the gimbal system has been fixed. In particular, if we define *Gimbal offset angle* δ the angle between the vertical direction and the current thrust direction, the range of values that this angle can assume has been limited to:

$$0° < |\delta| < 5° \tag{3.2}$$

This means that the cone of operation has an opening of 5°. In this way, the interference problems are avoided and, considering the angular actuation speed specified above, we can have a fast actuation in the whole work range since the entire angular displacement (10°) is covered in less than one second.

The main issue that can arise with this placement of the actuators is their relative vicinity with the exhaust gases of the engine. The maximum working temperature allowed for the actuators, as specified in table 3.2, is $65°C$ while the exhaust flow coming out of the nozzle can reach temperature around $750°C$. For this reason a thermal protection for the actuators may be needed.

3.5.3 Embedded electronics

The full embedded electronics system designed to drive and command all the different components of the TVC is given in the following block diagram:

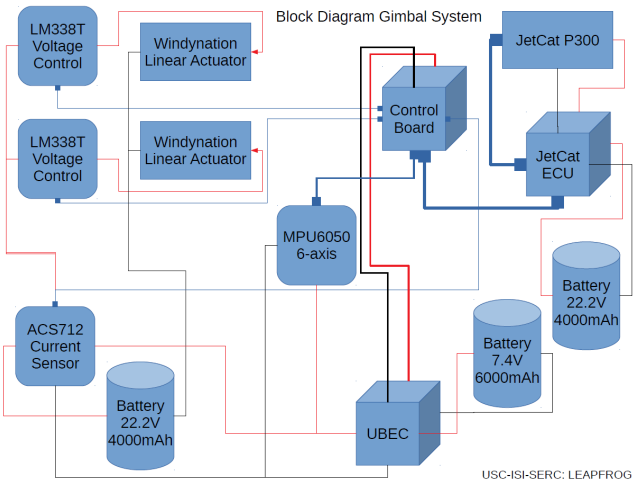

Figure 3.12: Thrust vectoring system embedded electronics

The red and black cables in the diagram represent an electric connection in which, in particular, red cables represent the positive pole and black cables represent the negative one. Blue cables, instead, represent a data connection between the different blocks.

The central core of the electronics system is represented by the control board, an Odroid CPU that exchanges information with LEAPFROG'S main CPU and IMU sensor. When the main CPU commands a variation of thrust vector amount, the control board feeds the information to the engine ECU that manages the engine performance. The power needed by the JetCat ECU and by the control board is furnished by a couple of LiPo batteries. In the case of the control board, the power coming from the battery is first processed by the UBEC block, a voltage regulator that feeds to the CPU a constant power with the proper values of voltage and current intensity. In the case, instead, in which the main LEAPFROG'S CPU commands an attitude adjustment maneuver, the control board, this time, communicates with the transistors that manage the on-off switching of the actuators. The transistors are identified by the 2 blocks LM338T Voltage control. Those components, in fact, according to the signal received by the control board, change the sign of the voltage given to the actuators, triggering the forward motion or the backward motion of the latter. The power needed by the actuators is furnished by a third LiPo battery. A current sensor is placed in the circuit in order to know the amount of current that is actually flowing. The battery used to power the actuators affects their performance

and can reduce their speed while the stored energy reduces and becomes a small amount. The last block sketched in the block diagram is a 6-axis IMU sensor. This extra IMU is placed on the inner ring of the gimbal joint and is used to have a feedback on the tilted position of the engine. The idea of the usage of this component came because the linear actuators employed are not equipped with a feedback loop that provides information on their displacement so, this extra sensor shows if the required engine position is achieved.

The full vehicle, with the different subsystems mounted on the structure, appears as shown below:

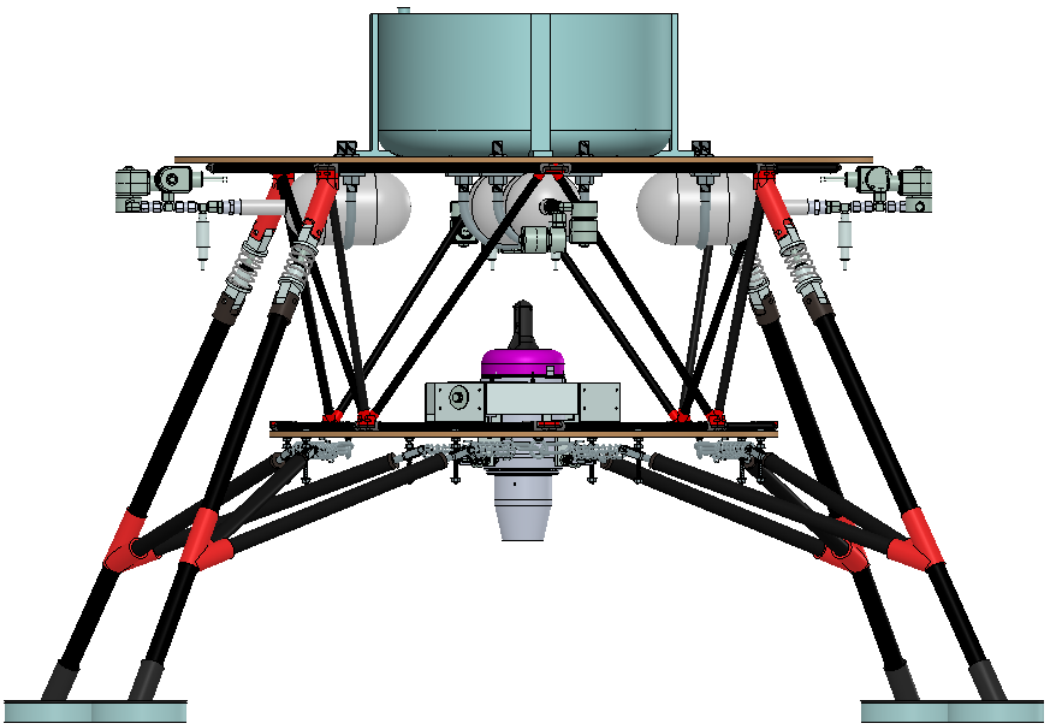

Figure 3.13: LEAPFROG Generation 2

The entire design phase had been followed by a budget analysis to keep track of the overall cost of the different parts and components selected for the prototype. The final sum showed a total cost for the entire vehicle around 10.000,00 $. Taking into account that the cost of the engine by itself is close to 5.000,00 $, we see that LEAPFROG represents a quite cheap solution among lunar lander simulators.

Chapter 4

Control system design

In the present chapter the dynamics of the system will be addressed and written down in terms of equations. After, the strategies used for the design of the control systems will be illustrated and described.

4.1 System Dynamics

As established in chapter 2, the rotational dynamics of a generic rigid body is described by the Euler equations. The described system, though, is not totally a rigid body since we have the relative motion of the engine with respect the full system. However, in the present work, since important information about the engine are not known, for sake of simplicity, the dynamics of the engine itself is not addressed and, instead, the effects of its motion are treated as external disturbances.

Writing down the Euler equations for the analyzed system, in the most general case, we get:

$$I\dot{\omega} = -\dot{I}\omega + (M_{atm} + M_{wind} + M_{dis} + M_{TVC} + M_{RCS} - \omega \times I\omega) \tag{4.1}$$

where M_{atm} and M_{wind} represent the external moments acting on the prototype due to drag force and presence of wind gust respectively, M_{dis} represents moments due to disturbances like fuel sloshing, M_{TVC} and M_{RCS} represent control torques exerted by, respectively, the thrust vectoring system and the reaction control system.

In the case of constant inertia, (4.1) simplifies to:

$$\dot{\omega} = I^{-1}(M_{atm} + M_{wind} + M_{dis} + M_{TVC} + M_{RCS} - \omega \times I\omega) \tag{4.2}$$

The aim of this work is to analyze the feasibility and the effectiveness of the designed

TVC system in order to understand which kind of improvements it can lead. To do that, an hovering condition of the prototype is simulated and the behaviour of the TVC is addressed in the function of attitude holding. Being the studied one a newly designed vehicle, the aerodynamic behaviour should be addressed with a deep CFD analysis. Due to lack of time, this analysis could not be performed. For this reason, having assumed an hovering condition of the prototype, the effect of the drag on the latter is assumed to be small and considered negligible. The analysis, instead, will be focused on the response of the vehicle to wind gusts and measurement uncertainties. Furthermore, now on, will be assumed that the pitch and yaw motion is fully controlled by the thrust vector control system while the roll motion, as already pointed out, due to TVC limitations, is fully controlled by the reaction control system. Assuming a full TVC actuation on yaw and pitch channels, we can analyze different scenarios and address what are the limitations of the gimbaled system, checking in which cases it can work by itself or in which cases it has to be synchronized with the RCS.

Considering those assumption, the Euler's equations can be written, projecting on the three axis, in this way:

$$\dot{\omega_x} = I_x^{-1}[M_{wind,x} + M_{dis,x} + M_{TVC,x} + (I_y - I_z)\omega_y\omega_z] \tag{4.3}$$

$$\dot{\omega_y} = I_y^{-1}[M_{wind,y} + M_{dis,y} + M_{TVC,y} + (I_z - I_x)\omega_z\omega_x] \tag{4.4}$$

$$\dot{\omega_z} = I_z^{-1}[M_{wind,z} + M_{dis,z} + M_{RCS,z} + (I_x - I_y)\omega_x\omega_y] \tag{4.5}$$

The different terms describing control torques exerted by the two control systems can be written down in analytic terms since they are known. For what concerns the RCS system, due to the particular placement of the thrusters shown in figure (3.5), the control torques given should projected on pitch and yaw axis since those are not aligned with principal axis of inertia. However, this problem doesn't arise in the roll channel, the only one in which the RCS is considered.

About the TVC, clearly, the two control torques applied on pitch and yaw motion are coupled since they are given by the same actuator (the engine). In order to write down the expression for those two control moments, we can decompose the thrust vector defining a particular set of spherical coordinates, represented in figure (4.1):

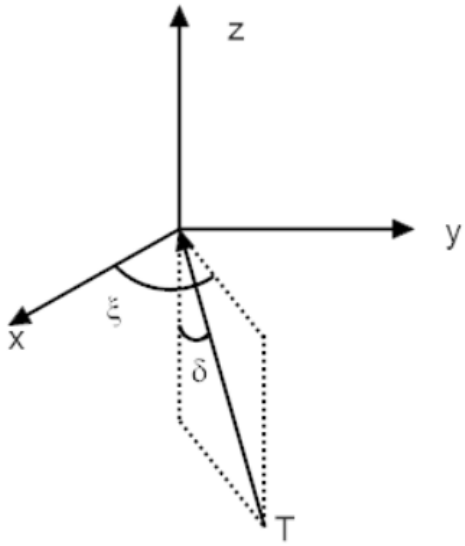

Figure 4.1: Thrust vector decomposition

where T represents the thrust vector, δ is the *gimbal offset angle* and ξ is defined the *gimbal rotation angle*. The notation used is the following:

- -90° $< \xi <$ 90°
- -5° $< \delta <$ 5°
- ξ is a positive rotation around $\hat{z}$
- $\xi = 0$ and $\delta > 0$ give a positive pitching moment (moment around $\hat{y}$)

According to figure 4.1, the components of the thrust along the three body axis are given by:

$$\vec{T} = T \begin{bmatrix} -sin\delta cos\xi \\ -sin\delta sin\xi \\ cos\delta \end{bmatrix} \tag{4.6}$$

and, consequently, the moments acting on the body are:

$$\vec{M_{TVC}} = Tl \begin{bmatrix} -sin\delta sin\xi \\ sin\delta cos\xi \\ 0 \end{bmatrix} \tag{4.7}$$

where l is the distance between the center of mass and the center of thrust. The center of thrust coincides with the gimbal rotation point.

Regarding the control torque of the RCS, with the assumption made above, it is given by:

$$\vec{M_{RCS}} = \begin{bmatrix} 0 \\ 0 \\ 2T_{th}r \end{bmatrix} \tag{4.8}$$

Where, T_{th} represents the thrust given by a single cold-gas thruster and r is the distance between the center of mass and the point of application of the thruster itself. Those quantities are multiplied by two since a rotation is controlled by two thrusters firing at the same time. Substituting (4.7) and (4.8) into (4.3), (4.4) and (4.5), we get:

$$\dot{\omega_x} = I_x^{-1}[M_{wind,x} + M_{dis,x} - Tlsin\delta sin\xi + (I_y - I_z)\omega_y\omega_z] \tag{4.9}$$

$$\dot{\omega_y} = I_y^{-1}[M_{wind,y} + M_{dis,y} + Tlsin\delta cos\xi + (I_z - I_x)\omega_z\omega_x] \tag{4.10}$$

$$\dot{\omega_z} = I_z^{-1}[M_{wind,z} + M_{dis,z} + 2T_{th}r + (I_x - I_y)\omega_x\omega_y] \tag{4.11}$$

About the attitude representation, in the following control system design a quaternion representation is chosen because of its numerical favorable properties and the uniqueness of its formulation.

4.2 Linear Quadratic Regulator

The first control system to be addressed is a classic LQR control system. This particular controller is part of the optimal control theory. A control system is defined optimal when, given some inputs, it gives the best performance possible [21]. This characteristics is reached by minimizing a particular cost function. An optimal controller is defined Linear Quadratic when the set of differential equations describing the dynamic system is characterized by linear equations and the cost function assumes a quadratic shape. The largest part of real-life dynamic systems are characterized by a non-linear behaviour so, theoretically, are not eligible for this kind of control system. However, what is usually done is to approximate the dynamic of the system around a trim point using linear equations [21], making possible the application of LQR control.

So, we see that optimal control theory is a very powerful tool since we can find the optimum gain that stabilizes our system. However, in general, the stability of the

system is only local, around the trim point. If the system moves away from this condition, linear control is no more valid so, with this particular control, we don't have a global stability of the system.

4.2.1 Cost function and Riccati equation

As already pointed out, LQR are applied to dynamic systems described by linear differential equations. In general, the set of linear equations can be written in state-space form:

$$\dot{x} = Ax + Bu \tag{4.12}$$

where x and u represent, respectively, the state vector and the input vector. The two matrices A and B are called state matrix and input matrix. This set of equations is usually completed by the output equations:

$$y = Cx + Du \tag{4.13}$$

The quadratic cost function, introduced before, to be minimized is the following:

$$J = \frac{1}{2}\int_0^\infty (x^T Q x + u^T R u)\, dt \tag{4.14}$$

Q and R are square diagonal matrices of dimension, respectively, $(n \times n)$ and $(m \times m)$ where n is the length of the state vector and m the length of the input vector. They are defined to b $Q \geq 0$ and $R > 0$ and represent the state and input penalization in the optimal control law.

The minimization problem is solved by the definition of the following Hamiltonian function [23]:

$$H = x^T Q x + u^T R u + \lambda^T (Ax + Bu) \tag{4.15}$$

The vector λ is defined co-state. The minimization problem leads to:

$$u = -R^{-1} B^T \lambda \tag{4.16}$$

This u represents the optimal input. From this expression we can see that, as specified above, R must be strictly > 0, otherwise it could not be inverted.

However, we need the definition of the optimum input in terms of the actual state. To do that, we assume that the shape of the co-state is the following:

$$\lambda(t) = S(t)x(t) \tag{4.17}$$

Consequently, deriving (4.17) and substituting (4.12) and (4.16), we get:

$$\dot{\lambda} = \dot{S}x + S(A - BR^{-1}B^T S)x \tag{4.18}$$

From the Hamiltonian function we can also get:

$$-\dot{\lambda} = Qx + A^T\lambda \tag{4.19}$$

and substituting into (4.18):

$$-\dot{S}x - SAx + BR^{-1}B^T Sx = Qx + A^T x \tag{4.20}$$

From which we derive the so called Riccati ordinary differential equation (ODE):

$$-\dot{S} = SA + A^T - BR^{-1}B^T S + Q \tag{4.21}$$

Solving the latter for S, we get the optimal control in terms of the state vector:

$$u(t) = -R^{-1}B^T S(t)x \tag{4.22}$$

This control law is time varying. However, it can be shown that for time reaching infinity, S becomes a constant. Consequently, the Riccati ODE becomes the Riccati Algebraic Equation:

$$0 = SA + A^T - BR^{-1}B^T S + Q \tag{4.23}$$

Solving which, we get a constant optimal input:

$$u = -R^{-1}B^T Sx \tag{4.24}$$

where

$$K_{opt} = R^{-1}B^T S \tag{4.25}$$

represents the optimal control gain.

We see that the solution of the Riccati equation provides the optimal control law that minimize the cost function (4.14). However, the solution of the Riccati equation is not always possible but exists only under certain conditions, which are:

1) $Q \geq 0$ and $R > 0$

2) The couple (A,C) is observable

3) The couple (A,B) is controllable

Those conditions are really important to point out since they underline a weakness of the quaternion attitude parameterization. Even though quaternion representation has several advantages, a linear model based on the all four components results to be non fully controllable, making the application of a classic LQR control not possible [35]. However, has been shown that a reduced quaternion model can be obtained by only considering the three vectorial components of the quaternion, leading to a completely controllable system.

4.2.2 Reduced quaternion model

Let's recall the non-linear attitude kinematics equations expressed in (2.27) and (2.28), considering q_4 as the scalar component of the quaternion and simply calling q the vectorial part of the quaternion:

$$\dot{q} = \frac{1}{2}\Omega' q + \frac{1}{2} q_4 \omega_b \tag{4.26}$$

$$\dot{q}_4 = -\frac{1}{2}\omega_b^T \vec{q} \tag{4.27}$$

In [34] is shown that there exists a one to one mapping between ω and $\dot{q}$ for which equations (4.26) and (4.27) can be replaced by a set of nonlinear attitude kinematics equations that can then lead to a linear dynamic system based on quaternion representation.

This mapping is given by:

$$\omega = 2\Theta^{-1}\dot{q} \tag{4.28}$$

Where:

$$\Theta = \begin{bmatrix} f(q) & -q_3 & q_2 \\ q_3 & f(q) & -q_1 \\ -q_2 & q_1 & f(q) \end{bmatrix} \tag{4.29}$$

The function composing the main diagonal of the matrix is defined as follow:

$$f(q) = \sqrt{1 - q_1^2 - q_2^2 - q_3^2} = q_4 \tag{4.30}$$

What's basically done is replace the 4th quaternion component with its expression in terms of the other three components.

The mapping between ω and $\dot{q}$ given in (4.28), however, is valid only when $\Phi \neq \pi/2$ where, as already illustrated in chapter 2:

$$[q^T, q_4]^T = [\hat{e}^T sin\frac{\Phi}{2}, cos\frac{\Phi}{2}]^T \tag{4.31}$$

Considering (4.28), we can replace (4.26) and (4.27) with the following set of equations:

$$\begin{bmatrix} \dot{q}_1 \\ \dot{q}_2 \\ \dot{q}_3 \end{bmatrix} = \frac{1}{2} \begin{bmatrix} f(q) & -q_3 & q_2 \\ q_3 & f(q) & -q_1 \\ -q_2 & q_1 & f(q) \end{bmatrix} \begin{bmatrix} \omega_1 \\ \omega_2 \\ \omega_3 \end{bmatrix} = g(q_1, q_2, q_3, \omega) \tag{4.32}$$

Recalling the generic expression of the Euler equations, with the assumption of constant inertia:

$$I\dot{\vec{\omega}} = u - \vec{\omega} \times I\vec{\omega} \tag{4.33}$$

where $u = [u1, u2, u3]^T$ represents the control torques vector in body axis, we can derive the final linear reduced quaternion model applying Taylor expansion to (4.32) and (4.33). Going through calculations, we can get the final expression of the linear system:

$$\begin{bmatrix} \dot{\omega} \\ \dot{q} \end{bmatrix} = \begin{bmatrix} 0_3 & 0_3 \\ \frac{1}{2}I_3 & 0_3 \end{bmatrix} \begin{bmatrix} \omega \\ q \end{bmatrix} + \begin{bmatrix} I^{-1} \\ 0_3 \end{bmatrix} u = Ax + Bu \tag{4.34}$$

Where 0_3 represents a 3×3 matrix of all zero components, I_3 is a 3×3 identity matrix and I is the inertia matrix. It can be demonstrated that the derived system is fully controllable, solving the typical issue of the full quaternion dynamics.

The derived model can be very useful when a linear analysis in terms of quaternion is wanted to be stressed out. It is widely used not only in spacecraft applications but also in Unmanned Aerial Vehicles (UAV) designed for multiple flight modes. Although, as underlined before, there is a singularity in which this model is no more valid (i.e. when $q_4 = 0$). In [19] is pointed out that this issue can be overcome by the application of an appropriate change of coordinates. However, as explained before,

in this work, the assessment of the behaviour of the TVC system is made through the simulation of an hovering working condition of the prototype. In this particular condition, the vehicle, in terms of attitude, is trimmed around the point:

$$\Theta = \begin{bmatrix} 0 \\ 0 \\ 0 \end{bmatrix} \; ; \; \omega = \begin{bmatrix} 0 \\ 0 \\ 0 \end{bmatrix} \tag{4.35}$$

where Θ represents the Euler angles.

The quaternion deriving from this set of Euler angles is $q = [0\ 0\ 0\ 1]^T$ so we see that we are sufficiently far from the critical condition $q_4 = 0$ to assume that the derived reduced quaternion model can be considered acceptable for our analysis.

4.2.3 Asymptotic stability

The optimal control law deriving from a linear quadratic minimization problem is really strong since it always leads to a closed-loop system asymptotically stable. This particular property can be proved via Lyapunov stability sense. To do that, we select a Lyapunov candidate function with this shape:

$$V = x^T P x, \; with \; P > 0 \tag{4.36}$$

Deriving (4.36):

$$\dot{V} = \dot{x}^T P x + x^T P \dot{x} \tag{4.37}$$

Substituting in (4.37) the closed-loop state space equation:

$$\dot{x} = (A - BK_{opt})x \tag{4.38}$$

and performing calculations, we arrive at the following expression:

$$\dot{V} = x^T(-Q - PBR^{-1}B^T P)x \tag{4.39}$$

In the formulation of the LQR problem is assumed that $Q \geq 0$ and $R > 0$. Moreover, in the definition of the Lyapunov candidate function, it was selected a matrix $P > 0$. This means that:

$$Q + PBR^{-1}B^T P > 0 \tag{4.40}$$

and consequently:

$$\dot{V} < 0 \tag{4.41}$$

proving the asymptotic stability of the closed-loop via Lyapunov sense. The exact formulation of Lyapunov stability theorem is illustrated in appendix A.

4.3 Sliding Mode Control

Non linear controllers have been widely investigated to fix the main weaknesses of linear controllers which have restricted range of actions, bad behaviour in presence of hard non-linearities and effects of non-modeled dynamics [30]. Sliding mode control, in particular, is well known for its ability to handle complex non-linear system that contains uncertainties and disturbances [17]. This control system is based on the definition of a sliding surface (also called sliding manifold) on the error space. It can drive the system to a desired state by taking it to the manifold and then converging the error to the origin maintaining the system to the manifold itself.

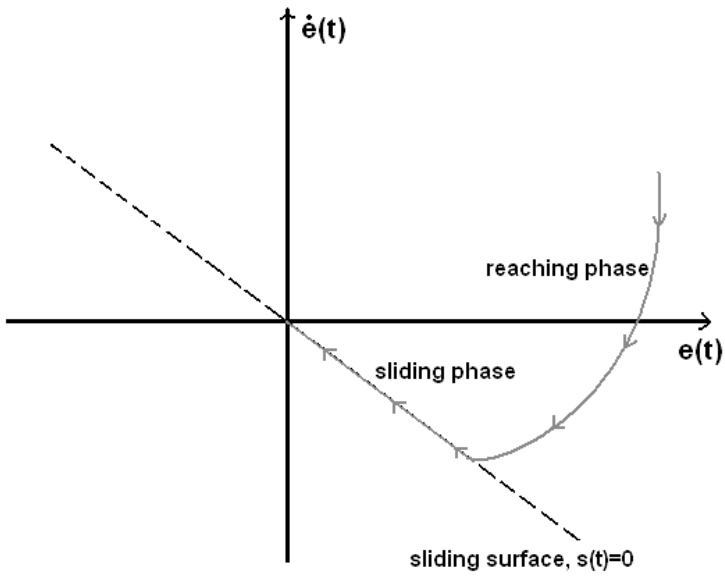

Figure 4.2: Ideal sliding mode [13]

The arrows depicted in figure (4.3) show the path followed by the system in the phase-plane, which starts from an initial configuration and, once got the sliding surface, slides till the desired condition.

4.3.1 Sliding manifold and control law definition

In order to design the sliding mode control law, the first step is the design of the sliding surface. Since we're dealing with an attitude problem, the sliding law will be given in terms of quaternion error and angular velocity error, given by the difference between the actual values and the desired one:

$$\bar{q}_e = \bar{q} - \bar{q}_d \tag{4.42}$$

$$\omega_e = \omega - \omega_d \tag{4.43}$$

The sliding manifold is define as follows:

$$S = Wq_e + \omega_e \tag{4.44}$$

where W is a positive diagonal matrix that gives a weight to the quaternion components. We have to notice that the quaternion appearing into the expression (4.44) is only the vectorial part, discarding the component q_4.

In order to find a stabilizing solution, following the same procedure that has been used to show the asymptotic stability of the LQR controller, the problem is analyzed via Lyapunov stability sense. To do that, also in this case, we define a candidate Lyapunov function with the following shape:

$$V = \frac{1}{2}S^T S \tag{4.45}$$

The dynamic equations describing the behaviour of q_e and ω_e, in the most general case, are the following:

$$\frac{dq_e}{dt} = \frac{1}{2}\langle q_e \times \rangle \omega_e + \frac{1}{2}q_{e4}\omega_e \tag{4.46}$$

$$\frac{dq_{e4}}{dt} = -\frac{1}{2}\omega_e^T q_e \tag{4.47}$$

$$I\dot{\omega} = -\dot{I}\omega - \langle \omega \times \rangle I\omega + T_d + d \tag{4.48}$$

T_d is the vector of the desired torques to stabilize the platform and d are the external disturbances torques. The disturbances term comprise any kind of disturbances that we can have acting on our system like aerodynamic disturbances, inertia and measurements uncertainties, sloshing of fuel inside tanks, relative motion of the

engine with respect the main structure, etc. This term is unknown but considered to be bounded, such that:

$$|d| \leq d^{max} \tag{4.49}$$

Proceding as in section 4.2.3, we derive the expression given in (4.45):

$$\dot{V} = S^T \dot{S} \tag{4.50}$$

Substituting (4.48) and the derivative of (4.44), we get:

$$\dot{V} = S^T[W(\frac{1}{2}\langle q_e \times \rangle \omega_e + \frac{1}{2} q_{e4}\omega_e) + I^{-1}(-\dot{I}\omega - \langle \omega \times \rangle I\omega + T_d + d) - \dot{\omega}_d] \tag{4.51}$$

The stability via Lyapunov sense is proved if:

$$\dot{V} < 0 \tag{4.52}$$

To obtain that we can choose an appropriate structure of the control torques vector T_d. A possible solution, as also illustrated in [36], is to use the following control torques:

$$T_d = I[\dot{\omega}_d - kS - W(\frac{1}{2}\langle q_e \times \rangle \omega_e + \frac{1}{2} q_{e4}\omega_e)] + \dot{I}\omega + \langle \omega \times \rangle I\omega + \tau \tag{4.53}$$

Where $\tau = -ksign(S)$ and $k = d^{max} + \eta$, with $\eta > 0$ a sufficiently big constant.
If we plug the expression of T_d given in (4.52) into (4.50), we get:

$$\begin{aligned}\dot{V} = S^T[W(\frac{1}{2}\langle q_e \times \rangle \omega_e + \frac{1}{2} q_{e4}\omega_e) + I^{-1}(-\cancel{\dot{I}\omega} - \cancel{\langle \omega \times \rangle I\omega} + ... \\ ... + I[\dot{\omega}_d - kS - W(\frac{1}{2}\langle q_e \times \rangle \omega_e + \frac{1}{2} q_{e4}\omega_e)] + \cancel{\dot{I}\omega} + \cancel{\langle \omega \times \rangle I\omega} + \tau + d) - \dot{\omega}_d]\end{aligned} \tag{4.54}$$

Keeping going with calculations and semplifications, we arrive at the final expression of $\dot{V}$, which is:

$$\dot{V} = -S^T kS - |S^T| I^{-1}(k - |d|) < 0 \tag{4.55}$$

Proving that the chosen control law leads to an asymptotically stable system. In terms of sliding mode control, this means that, once the system reaches the sliding

manifold, it is forced to remain on it [36].

In particular, since in the present work we are simulating an hovering condition, the desired quaternion and desired angular velocity are constant in time so $\dot{q}_d = 0$ and $\dot{\omega}_d = 0$. For this reason, in our case, the control torques law can be simplified to:

$$T_d = I[-kS - W(\frac{1}{2}\langle q_e \times \rangle \omega_e + \frac{1}{2} q_{e4} \omega_e)] + \dot{I}\omega + \langle \omega \times \rangle I\omega + \tau \tag{4.56}$$

A further semplification can be achieved in the case of constant moments of inertia:

$$T_d = I[-kS - W(\frac{1}{2}\langle q_e \times \rangle \omega_e + \frac{1}{2} q_{e4} \omega_e)] + \langle \omega \times \rangle I\omega + \tau \tag{4.57}$$

4.3.2 Chattering phenomenon

As already pointed out, the variable structure of SMC, allows it to force the controlled system to reach, from any point in the error phase plane, the sliding surface. A typical Lyapunov derived control input is characterized by the following structure [17]:

$$u(t) = u_{eq} + u_{dis} \tag{4.58}$$

Where, in our case, it is:

$$u_{dis} = \tau = -ksign(S) \tag{4.59}$$

A characteristic of sliding mode controllers, is that, once the system reaches the sliding manifold, the u_{dis} component of the control input is forced to switch at infinite frequency to keep the system on the sliding manifold. This particular drawback of the SMC is referred to as *chattering* [15] [17]. We can see, then, that the behaviour showed in figure 4.3 is the ideal one, not reachable with the classic formulation of the sliding mode control law.

Depicted in figure 4.4 the typical behaviour of the system under chattering effect. We can see that this phenomenon starts showing itself as soon as the system reaches the sliding manifold and starts sliding onto it.

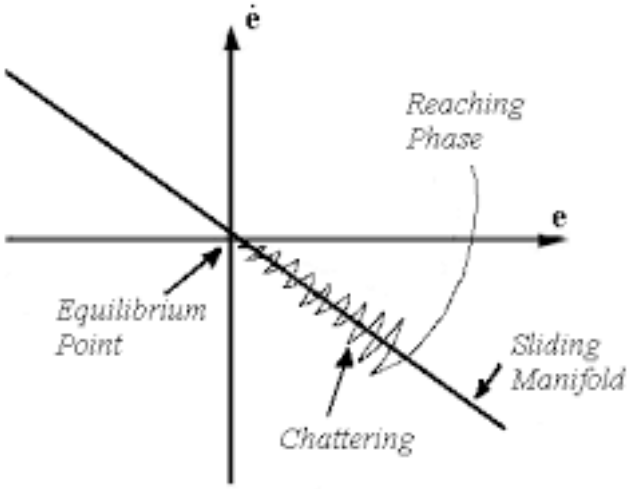

Figure 4.3: Chattered sliding mode [12]

This phenomenon is really unwanted since it may cause different problems. Among those, the most critical are the following:

- High frequency switching of actuators can lead to a degradation of mechanical components.
- High frequency switching can excite unmodeled dynamics and lead to undesired system performances.

Moreover, the particular structure of the actuation plant used in the presented TVC system, described in chapter 3, could not handle a too high frequency switching so, for this reason, chattering as to be avoided.

One of the solutions often adopted, is the application of the so called *Boundary Layer sliding mode control*, introduced for the first time in [29]. This method is based on the linearization of the SMC in a predefined boundary β of the sliding manifold and the resulting controller is characterized by a saturation function that replaces the sign function. This particular function is defined as follows:

$$sat(S) = \begin{cases} S/\beta \ for \ |S| < \beta \\ sign(S) \ for \ |S| \geq \beta \end{cases} \tag{4.60}$$

Where we recall that S represents the analytic expression of the sliding manifold.

What basically happens with the application of this equation is that, when $|S| \geq \beta$, the characteristic shape of the SMC law ensures that the system reaches the sliding manifold. Once the system sits on the sliding surface and $|S| < \beta$, the saturation function avoid the discontinuity of the system and cancels out the chattering problem. However, the introduction of the boundary layer reduces the reaching property of the SMC since the system would be confined in a small region around the manifold rather than reaching exactly $S = 0$.

Another possible solution for chattering attenuation is presented in [27]. This method contemplate the approximation of the sign function with a smoother one called *sigmoid function*, characterized by the following analytical expression:

$$sign(S) \approx \frac{S}{|S| + \sigma} \tag{4.61}$$

where σ is a small positive scalar. We can see that:

$$\lim_{\sigma \to 0} \frac{S}{|S| + \sigma} = sign(S) \tag{4.62}$$

This means that, lower is the value of σ and closer will be the sigmoid function to the sign one. The choice of this value should be carried out through a trade off between an ideal performance and a smooth control action. As for the case of the boundary layer technique, the price that we pay for a smoother control is a reduction of robustness and accuracy. However, the performance of the smooth control law is not so distant from the one we get with the ideal discontinuous actuation. For this reason the control law derived with the usage of the sigmoid function is usually defined *quasi-sliding mode control* and the behaviour of the system is defined *quasi-sliding mode* [27].

In the presented work, the sigmoid function method has been adopted for chattering removal.

Chapter 5

Control system simulation

In this final chapter, the two control algorithms I am proposing are simulated in MATLAB/Simulink environment in order to assess their effectiveness and the feasibility of the implementation of the Thrust Vector Control system. The different results are then compared and discussed.

5.1 Input parameters

The main parameters used for the simulations are the known hardware characteristics that will be employed on the vehicle. Prior to full integration of the flight vehicle, the mass property values come from the CAD design. Inertia data are referred to principal axis of inertia. To obtain coefficients as realistic as possible, the entire CAD model has been built applying, for each component, the actual material used for the final hardware. The different parameters are all listed in the following table:

Table 5.1: Simulations input parameters

Input parameters	Values
Prototype mass [kg]	22,3
Prototype inertia [kg m^2]	[4.59 4.59 5.3]
Engine thrust [N]	218,7
Center of mass position [m]	[0 0 0]
Center of thrust position [m]	[0 0 -0.35]
Mass variation [kg/s]	-9.51×10^{-3}
Gimbal max angular velocity [rad/s]	0.3218

The thrust value adopted is the thrust needed to hover (i.e. equal to the weight of the prototype), since we're assuming that particular working condition. In addition, since we're analyzing the behaviour of the designed TVC system, the roll motion is assumed to be stabilized by the reaction control system for simplification. To get a stable system, in the simulations, virtual inputs are used for the control of pitch and yaw motion, where those inputs are given in terms of gimbal angles. Furthermore, the small mass variation allows us to assume the total mass stays constant in our short simulation time.

5.2 LQR controller simulations

The first control system to be analyzed is the linear quadratic control, designed for the linear system:

$$\begin{cases} \dot{x} = Ax + Bu \\ y = Cx + Du \end{cases} \tag{5.1}$$

The matrices A and B come from the reduced quaternion model described in section 4.2.2. Namely:

$$A = \begin{bmatrix} 0 & 0 & 0 & 0 & 0 & 0 \\ 0 & 0 & 0 & 0 & 0 & 0 \\ 0 & 0 & 0 & 0 & 0 & 0 \\ \frac{1}{2} & 0 & 0 & 0 & 0 & 0 \\ 0 & \frac{1}{2} & 0 & 0 & 0 & 0 \\ 0 & 0 & \frac{1}{2} & 0 & 0 & 0 \end{bmatrix} \tag{5.2}$$

and

$$B = \begin{bmatrix} I_x^{-1} & 0 & 0 \\ 0 & I_y^{-1} & 0 \\ 0 & 0 & I_z^{-1} \\ 0 & 0 & 0 \\ 0 & 0 & 0 \\ 0 & 0 & 0 \end{bmatrix} \tag{5.3}$$

where the state vector is $x = [\omega_x \ \omega_y \ \omega_z \ q_1 \ q_2 \ q_3]^T$ and the input vector is $u =$

$[T_x\ T_y\ T_z]$, namely the control torques acting on the three different axis. T_x and T_y are the torques exerted by the TVC system.

Concerning matrices C and D, we have to consider the sensors system of the prototype. IMU senses variation of Euler angles from which, through CPU calculation, we can register also angular velocity data. For this reason the matrices used are:

$$C = \begin{bmatrix} 1 & 0 & 0 & 0 & 0 & 0 \\ 0 & 1 & 0 & 0 & 0 & 0 \\ 0 & 0 & 1 & 0 & 0 & 0 \\ 0 & 0 & 0 & 1 & 0 & 0 \\ 0 & 0 & 0 & 0 & 1 & 0 \\ 0 & 0 & 0 & 0 & 0 & 1 \end{bmatrix} \tag{5.4}$$

and

$$D = \begin{bmatrix} 0 & 0 & 0 \\ 0 & 0 & 0 \\ 0 & 0 & 0 \\ 0 & 0 & 0 \\ 0 & 0 & 0 \\ 0 & 0 & 0 \end{bmatrix} \tag{5.5}$$

After a quick analysis to verify that the system is completely controllable and completely observable, in order to solve the cost function minimization problem, the matrices Q and R had to be designed. The structures used for the two matrices are:

$$Q = \begin{bmatrix} k & 0 & 0 & 0 & 0 & 0 \\ 0 & k & 0 & 0 & 0 & 0 \\ 0 & 0 & k & 0 & 0 & 0 \\ 0 & 0 & 0 & kc & 0 & 0 \\ 0 & 0 & 0 & 0 & kc & 0 \\ 0 & 0 & 0 & 0 & 0 & kc \end{bmatrix} \ ; \ R = \begin{bmatrix} r & 0 & 0 \\ 0 & r & 0 \\ 0 & 0 & r \end{bmatrix} \tag{5.6}$$

The three different coefficients have been designed by trial and error approach, trying to reach the best behaviour of the system keeping the needed gimbal angle as small as possible. The final values obtained are: $k = 2.5$, $c = 150$ and $r = 9$.

5.2.1 Ideal case

The first scenario analyzed to address the effectiveness of the control system is a disturbance-free condition in which the gimbal system has to restore the desired attitude starting from an initial offset condition. The first case addressed is a pure pitch motion (i.e the offset from the desired attitude is assumed to be present only in the pitch channel). The initial conditions considered are the following:

Table 5.2: Initial conditions

Initial conditions	Values
θ_0	$11.46°$ (0.2 rad)
q_0	$5.7296°/s$ (0.1 rad/s)

where q represents the pitch rate. The results obtained are given below:

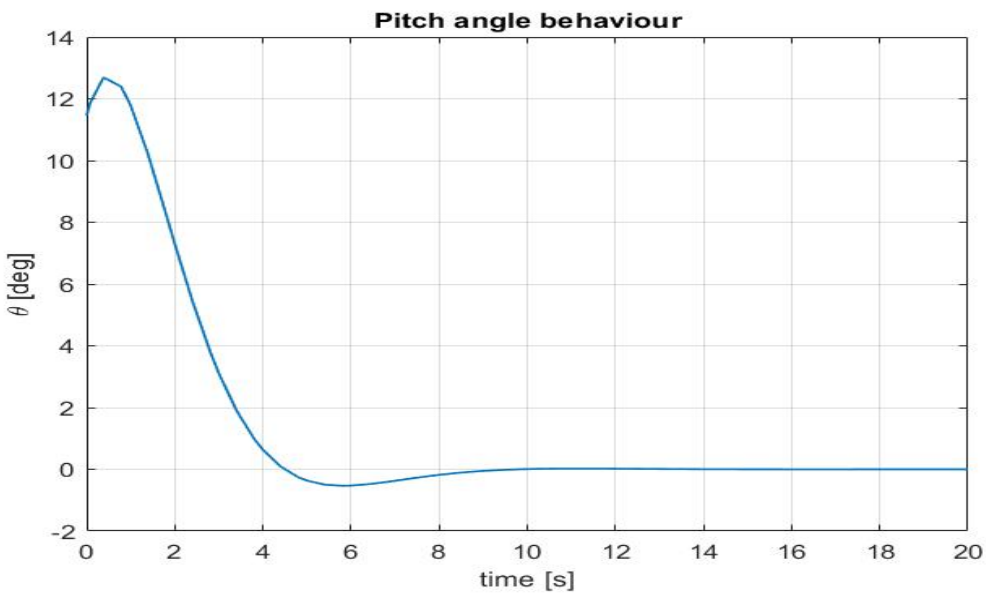

Figure 5.1: Pitch angle control

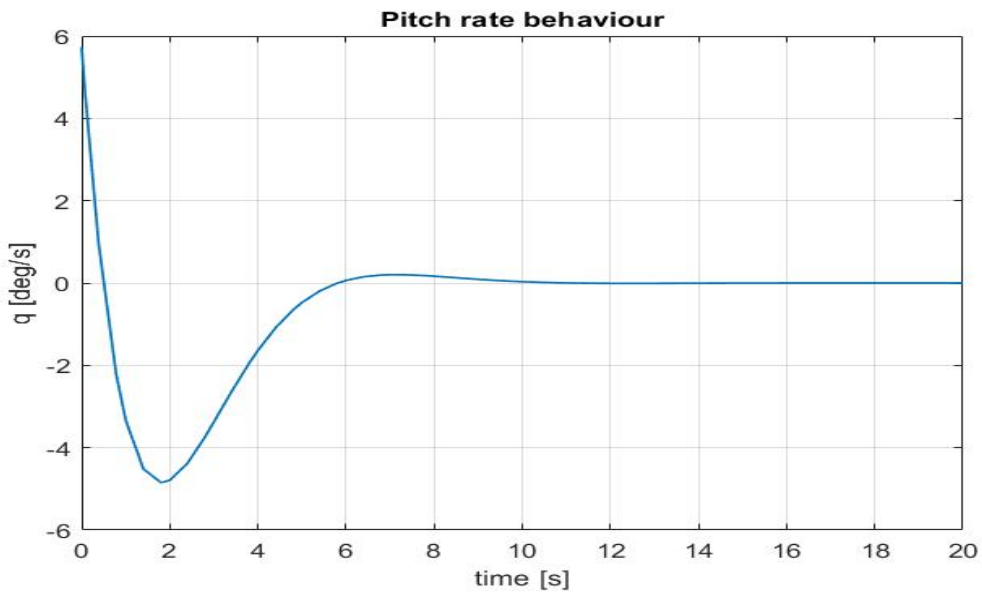

Figure 5.2: Pitch rate control

We can see that the designed controller restores the desired attitude conditions in almost 10 seconds. The gimbal angles needed to take pitch angle and pitch rate to zero are given below:

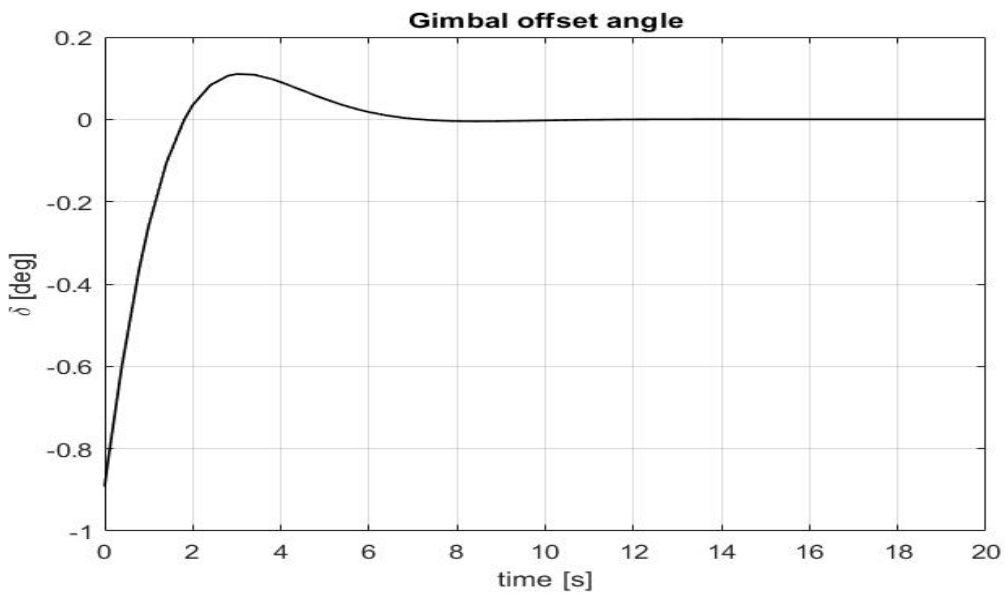

Figure 5.3: Gimbal offset angle δ

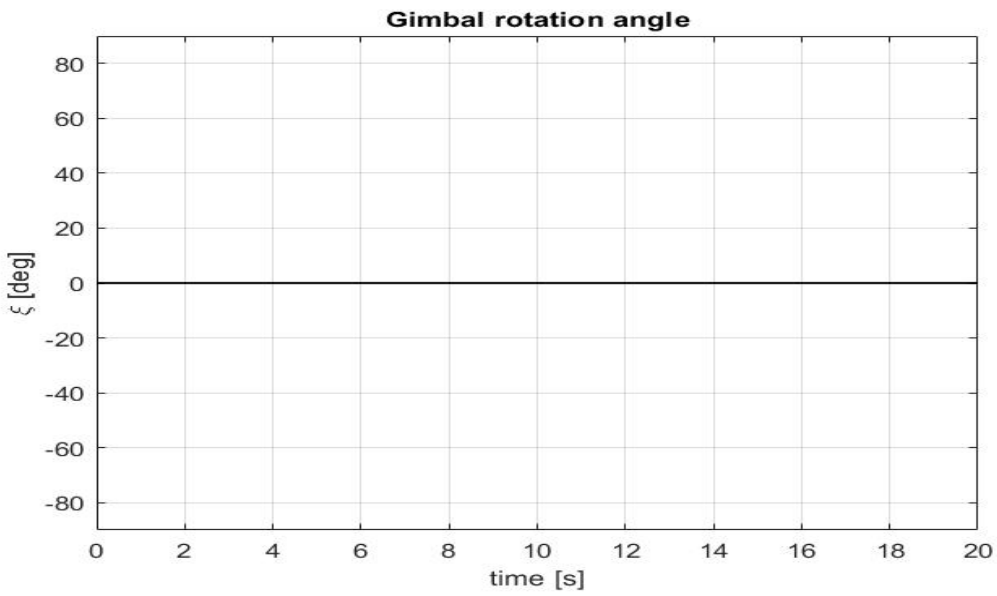

Figure 5.4: Gimbal rotation angle ξ

From figure (5.3) we can see that the displacement of the engine needed to cancel out the attitude error is totally inside the predefined working range of the angle δ. Moreover, calculation give that the distance between the two extreme points in graph (5.3) is:

$$\Delta\delta = 1.002^\circ \tag{5.7}$$

As we can see, this angular variation occurs in about 3 seconds so it's totally manageable by the TVC system. The particular behaviour of the angle ξ depicted in figure (5.4) is expected because, from the definition of the two angles, we have that $\xi = 0$ in case of pure pitch motion (Figure 4.1). The designed controller accomplished it's main purpose to stabilize the system with a reduced amount of engine angular displacement.

5.2.2 Perturbed case

In order to assess how the control system reacts to external disturbances, two different cases have been analyzed:

1) Presence of external impulsive disturbances

2) Presence of external random noise

The first case addressed is the system perturbed by an external impulsive disturbance. The system is assumed to be in a stable position and then displaced by an external impulse. To simulate this situation, a one second long half-sine unitary impulse has been generated and used as input for the system.

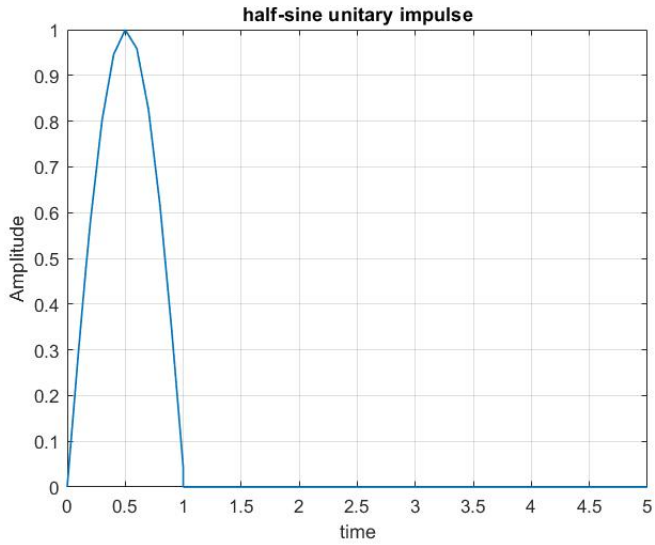

Figure 5.5: Half-sine unitary impulse

Assuming the half-sine impulse affecting only the pitch motion, the response of the system to this kind of perturbation is the following:

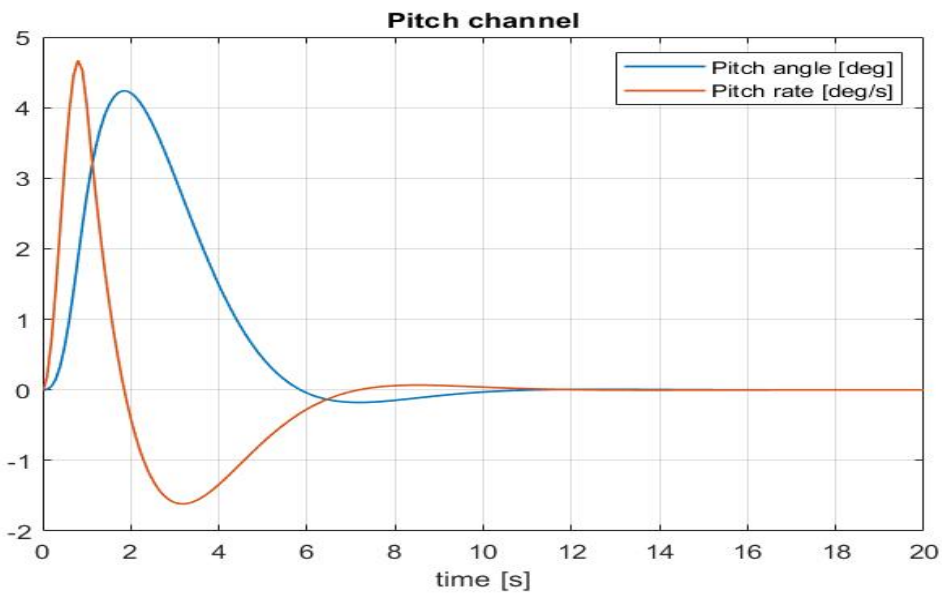

Figure 5.6: Pitch channel

The gimbal angle δ needed to dampen the system is shown below:

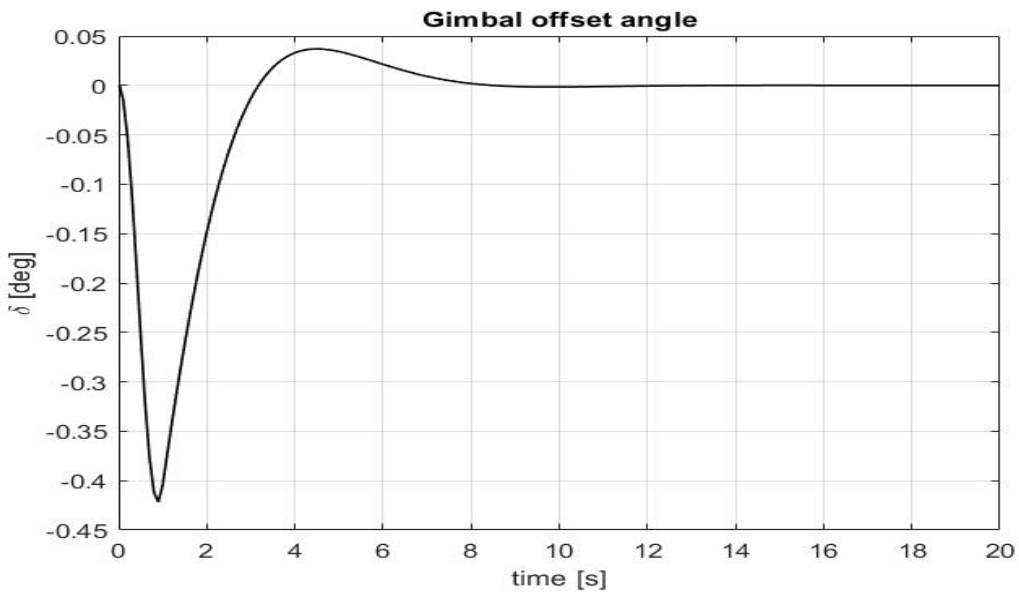

Figure 5.7: angle δ - impulse response (pitch)

Clearly, also in this case, the angle ξ is equal to zero for the same reasons as before. We can see that the control system reacts quite well to impulse disturbances, needing only a small tilting of the engine. If we assume the perturbation present in both pitch and roll channel, we obtain the same damped behaviour as the one pictured in Figure (5.6), in both the cases. However, in this case, the angles needed are the following:

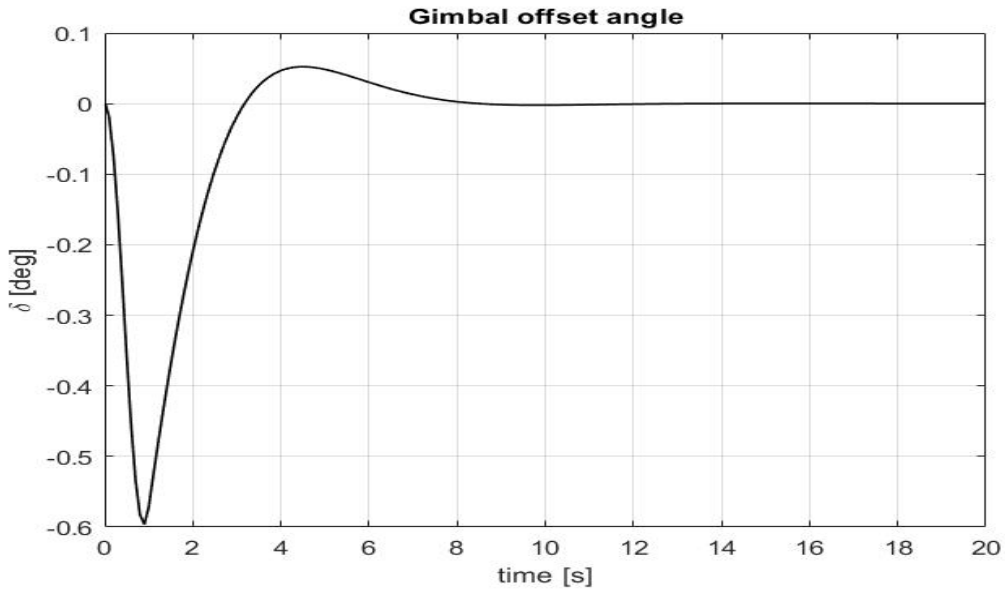

Figure 5.8: angle δ - impulse response (pitch and yaw)

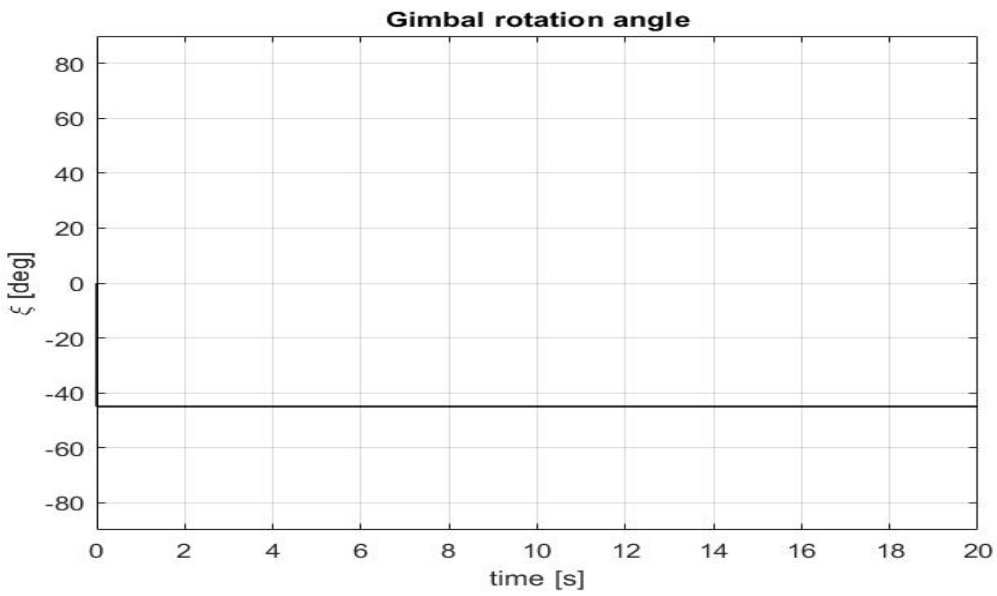

Figure 5.9: angle ξ - impulse response (pitch and yaw)

The first thing to notice is the behaviour of the angle ξ. As we may expect, the action of the TVC system happens in correspondence of $\xi = -45°$. This happens because, since the disturbance in yaw and pitch motion is the same, the same amount of control torque has to be given to both in order to stabilize the attitude. For the same reason, we can see that the displacement of the engine (*angle* δ) is bigger with respect the case of pure pitch control, since the torque generated by the engine is distributed in different channels. The negative sign in ξ is only due to the particular notation used.

In general, we can see that the controller presents an acceptable behaviour in presence of impulsive disturbances, stabilizing the system in roughly 10 seconds.

The second disturbance analysis concerns the presence of a random noise input. Let's assume same initial conditions as stated in table 5.1, adding a noise perturbing all the three rotations. A random external noise, for example, can represent a not-impulsive wind gust that interacts with the prototype. The particular geometry makes the assessment of the behaviour of the prototype under windy conditions a hard task. For this reason those conditions are considered as non-modeled dynamics in our system and, consequently, it is interesting to see how the LQR controller manages them. Another disturbance input could be a white noise that corrupts the state measurements that may be hardware induced.

The first test is the analysis of the response of the system to random external inputs. The latter are obtained from a random white noise that is fed into a generic transfer function for the generation of a correlated noise (coloured noise). The choice of

the application of a coloured noise instead of a white noise is due to the fact that real external disturbances, like wind, are more close to a correlated noise than a white one. The correlated noise analyzed is characterized by the following transfer function and value of root mean square deviation:

$$H(s) = \frac{1}{3s+1} \; ; \; RMS = 0.1 \tag{5.8}$$

In addition, for both the angular motion, initial conditions are set as the one given in Table 5.2. The effects of this noise on the system are shown below:

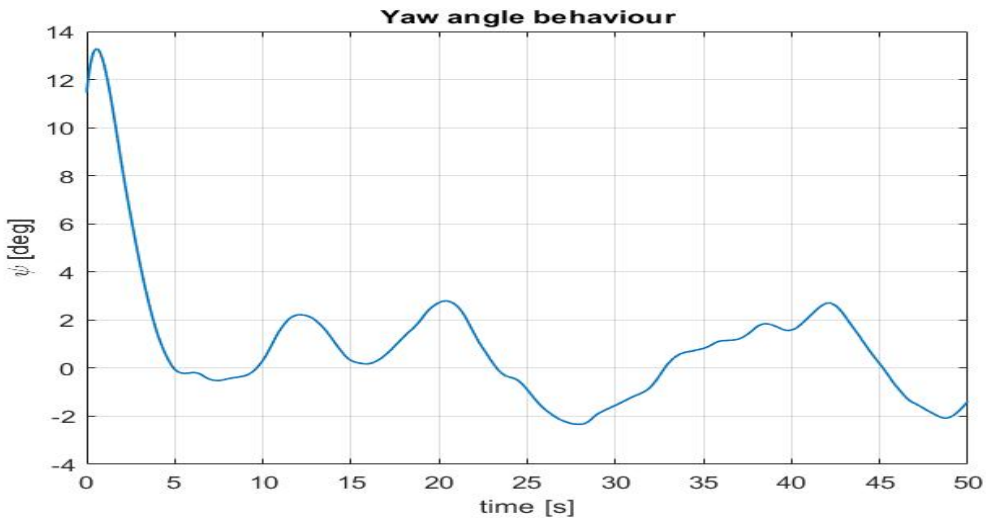

Figure 5.10: Yaw channel - external random noise

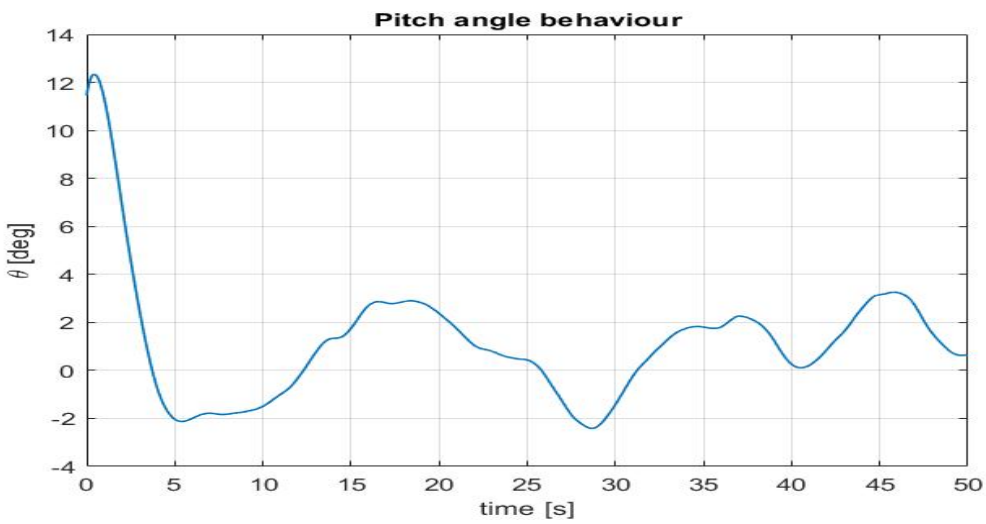

Figure 5.11: Pitch channel - external random noise

We can see that the generated noise results in angular displacement that can reach almost 4°, even if the LQR control tries to track the noise to keep it close to the

desired state. We can then say that this type of controller doesn't have a strong robustness to non-modeled dynamics. If we look in particular at the actuation system, the gimbal angles needed to restore the commanded attitude are the following:

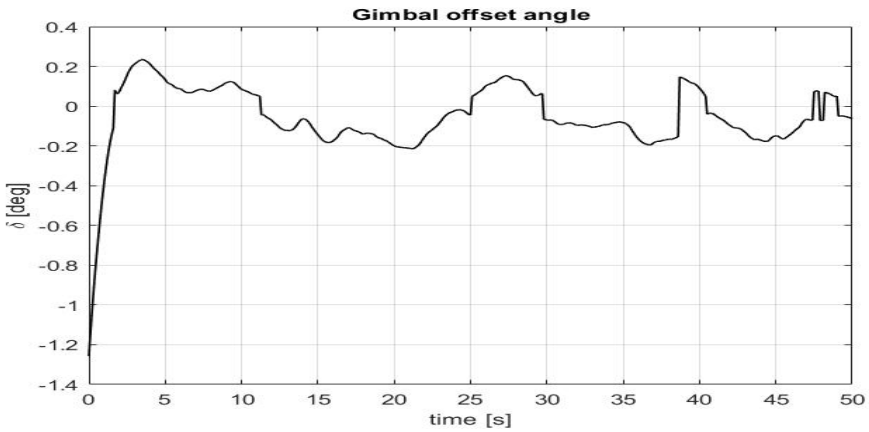

Figure 5.12: Angle δ in presence of random noise

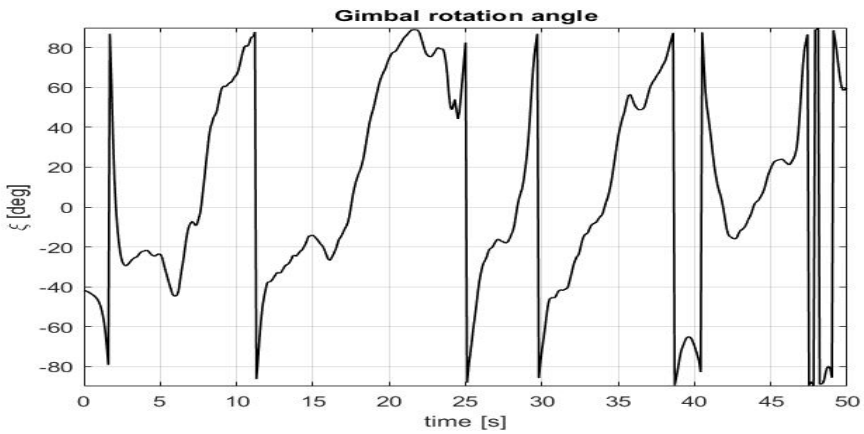

Figure 5.13: Angle ξ in presence of random noise

The gimbal offset angle can manage the external noise remaining in a small range of values. However, from the gimbal rotation angle we see that an high number of sudden changes of direction are happening. Anyway, the particular graph showing the angle ξ can mislead the interpretation since those high values of angles are not to be analyzed with the same approach based on actuation angular velocity used for the angle δ. In fact, if we translate those spherical coordinates into actuator displacement, we have those results:

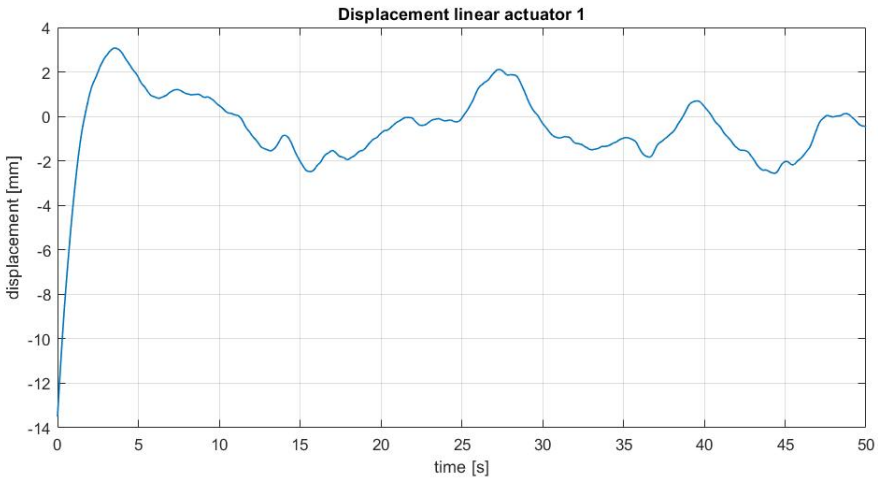

Figure 5.14: Displacement linear actuator 1

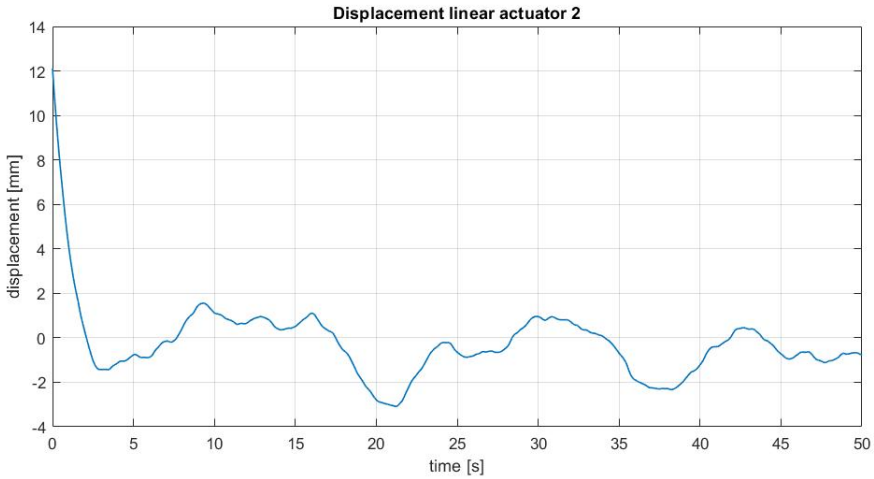

Figure 5.15: Displacement linear actuator 2

Looking at figures 5.14 and 5.15 we can have a better overview of what is going on in presence of random noise. To manage the disturbance, the TVC system needs, after the initial transient due to the initial conditions, just a small amount of linear displacement by the actuators. The latter are characterized by a speed of 30 mm/s (as assumed before) so they can handle the fast motion needed to control the vehicle. However, a couple of problems arise:

1) The actuators, even though could handle the motion in terms of speed, are limited by their duty cycle. As specifications from the manual, they have a duty cycle of 25% percent. This means that a too long perturbation could cause the overload of the actuators, leading to failure

2) The resolution of the actuators is not well know and should be tested in lab with the engine fired. In fact, they're resolution could not be small enough to allow particular small movements as the one that sometimes are needed here.

The second noise test is performed generating random errors in state measurements. Those random errors are generated by Gaussian distributed white noises affecting measurements in Euler angles and in angular velocity. As initial condition, the values presented in table 5.2 are used both for pitch and yaw channels. The standard deviations used for those errors are, in terms of degrees and degrees/s:

Table 5.3: Standard deviations

State variables	Standard deviation
Θ (Euler angles)	$2°$
ω (angular velocity)	$0.2°/s$

The results obtained are the following:

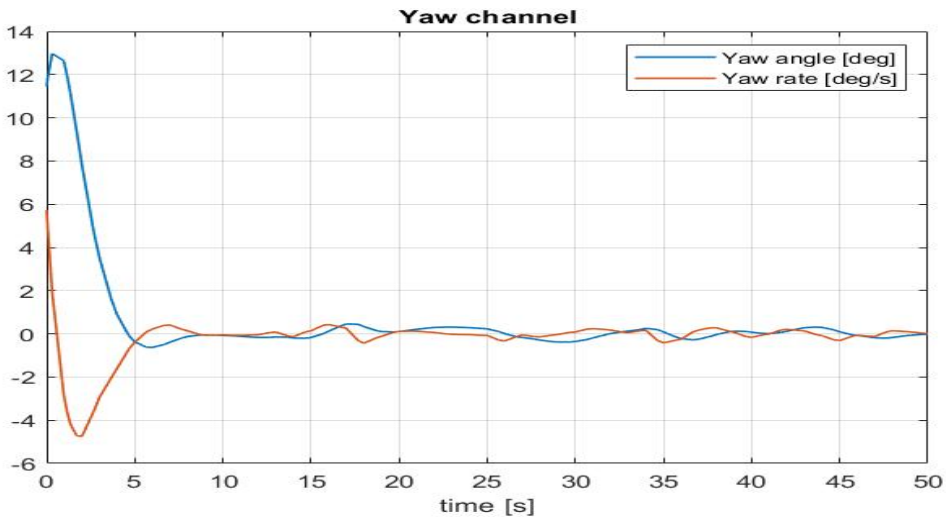

Figure 5.16: Yaw channel - presence of state measurements errors

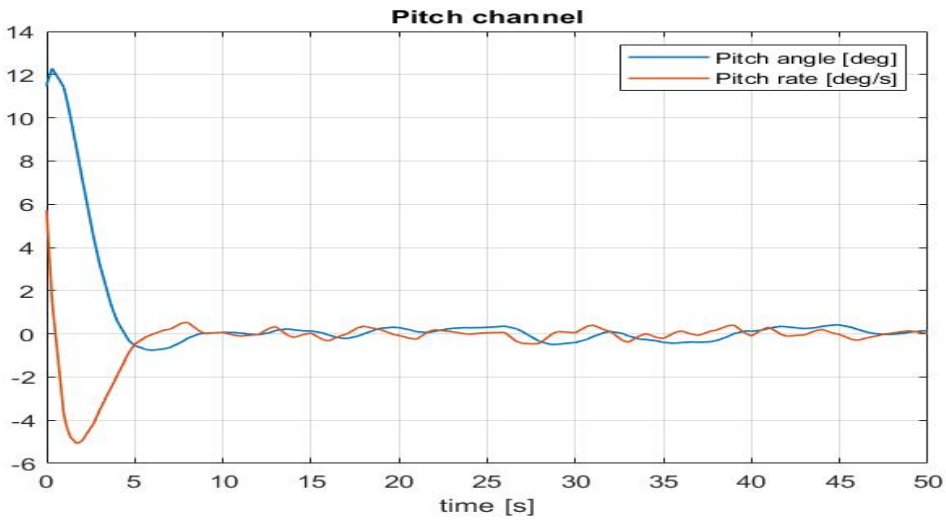

Figure 5.17: Pitch channel - presence of state measurements errors

We can see that the LQR controller behaves quite good in presence of measurements error since the desired state is not affected by them that much.
Once the behaviour and effectiveness of the control system is addressed, a further analysis concerning the verification of the employment of the TVC system was done. In particular, the final goal was to control, starting from different initial conditions, how many times the requested gimbal offset angle would be in the designed working range and, how many times it would have exceeded that. For this purpose, a set of 350 different initial conditions have been generated randomly to verify the relative engine tilting angle in a Monte Carlo analysis. To generate the random initial values some boundary conditions have been considered. In particular the Euler angles and the angular velocities generated have been restricted to the following ranges:

$$-60^\circ < \Theta_0 < 60^\circ \tag{5.9}$$

$$-20^\circ/s < \omega_0 < 20^\circ/s \tag{5.10}$$

where Θ represents the Euler angles and ω the body angular velocity.
The inputs have been randomly generated in MATLAB and then fed into Simulink environment for the simulation. The angles of interest analyzed are pitch and yaw angle, since those are the angles controllable with TVC system, and the gimbal offset angle.
The results obtained for pitch and yaw angles are depicted in following figures:

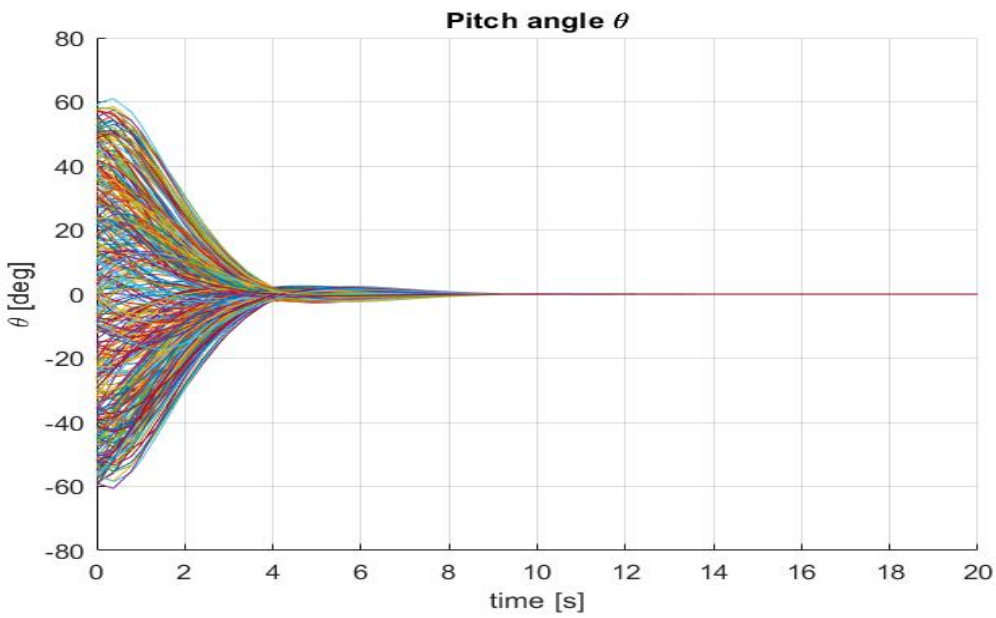

Figure 5.18: Pitch angle - different scenarios

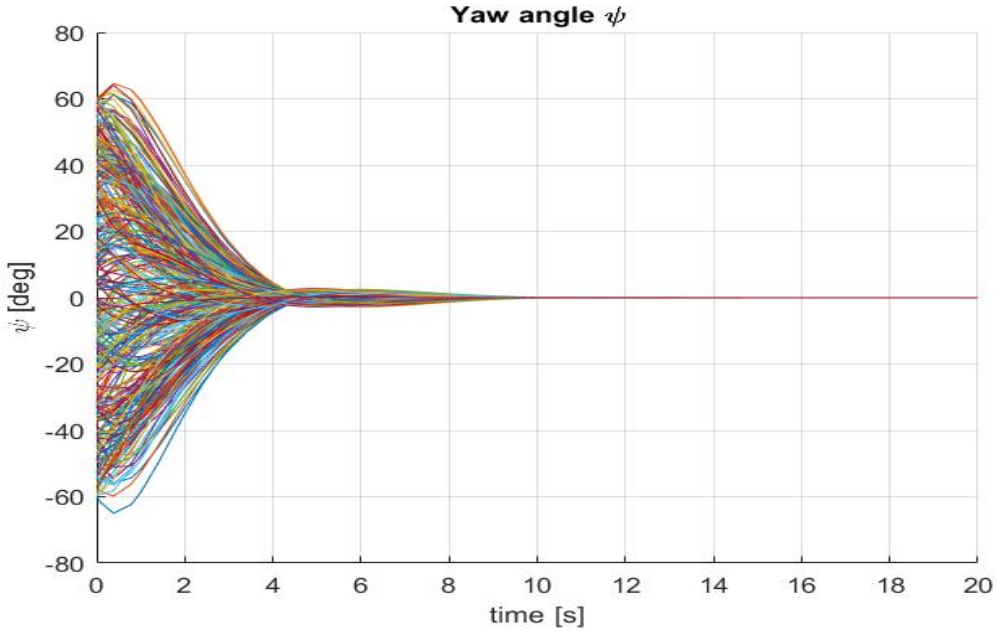

Figure 5.19: Yaw angle - different scenarios

We can see that, for both the angles, the control law stabilizes all the different random-generated initial conditions, reaching the desired state in about 10 seconds. The interesting result is the one relative to the gimbal angle, illustrated below:

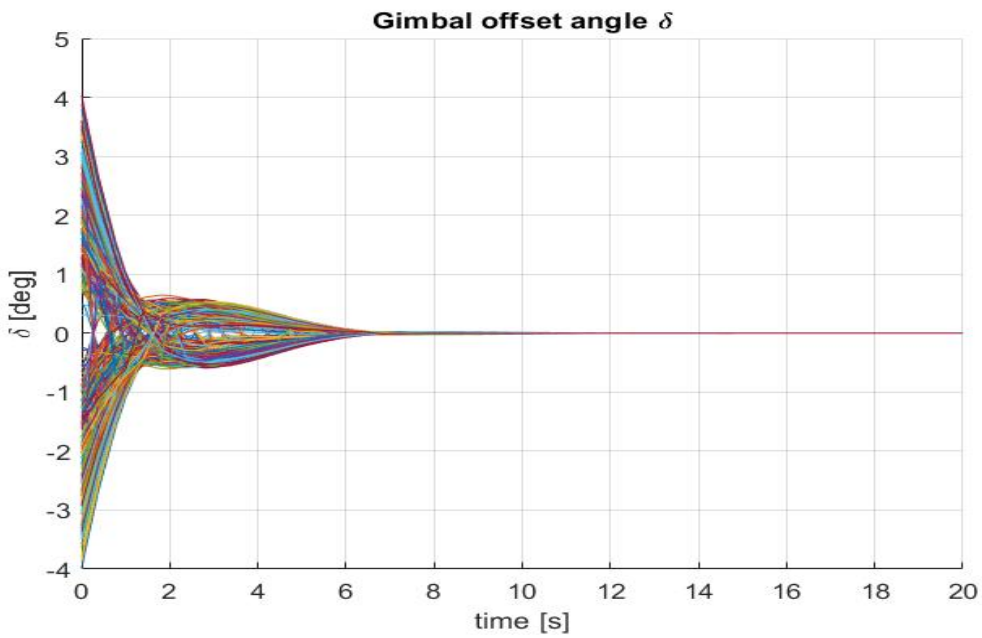

Figure 5.20: Gimbal offset angle - different scenarios

Looking at figure (5.7) we can say that the designed working range for the TVC system is sufficient for the re-balancing of the vehicle. However, always from this graph, we see that we are at the limits of the range ($-5° < \delta < 5°$). This means that bigger angular displacement or the presence of higher angular velocities would require an angle δ bigger than the allowable one. Consequence of this is that a full actuation with the TVC system is not possible since, for larger displacement, the usage of the reaction control system would be required.

5.3 Sliding mode controller simulations

The analysis exerted for the LQR system is replicated for the sliding mode control. This controller is based on the equation (4.56). To apply the control law, however, we have to design the matrix W and the constant k. The matrix W is the weight matrix for the quaternion variables while k, as already mentioned before, is defined as $k = d^{max} + \eta$. Concerning the design of k, since the dynamics of the system is not well defined, thus is hard to assess the maximum disturbance value to use. However, considering the analysis done for the LQR controller, we can take the maximum value of the perturbations applied to the model and use it as upper bound, adding the positive constant η according to the behaviour we want to reach. Trial and error approach have been applied to the design of the constant, leading to:

$$W = \begin{bmatrix} 1 & 0 & 0 \\ 0 & 1 & 0 \\ 0 & 0 & 1 \end{bmatrix} \tag{5.11}$$

$$d^{max} = 1 \ ; \ \eta = 0.2 \ ; \ k = 1.2 \tag{5.12}$$

The main problem with the unknown dynamics is that, in order to design the sliding mode controller, one has to overestimate the upper bound of the disturbances in order to avoid instability problems, increasing consequently the gain k. The higher is this gain, the higher will be the unwanted chattering phenomenon. If we apply those parameters to a classic sliding mode control, we obtain the following phase-plane plot, where the chattering phenomenon is clearly evident:

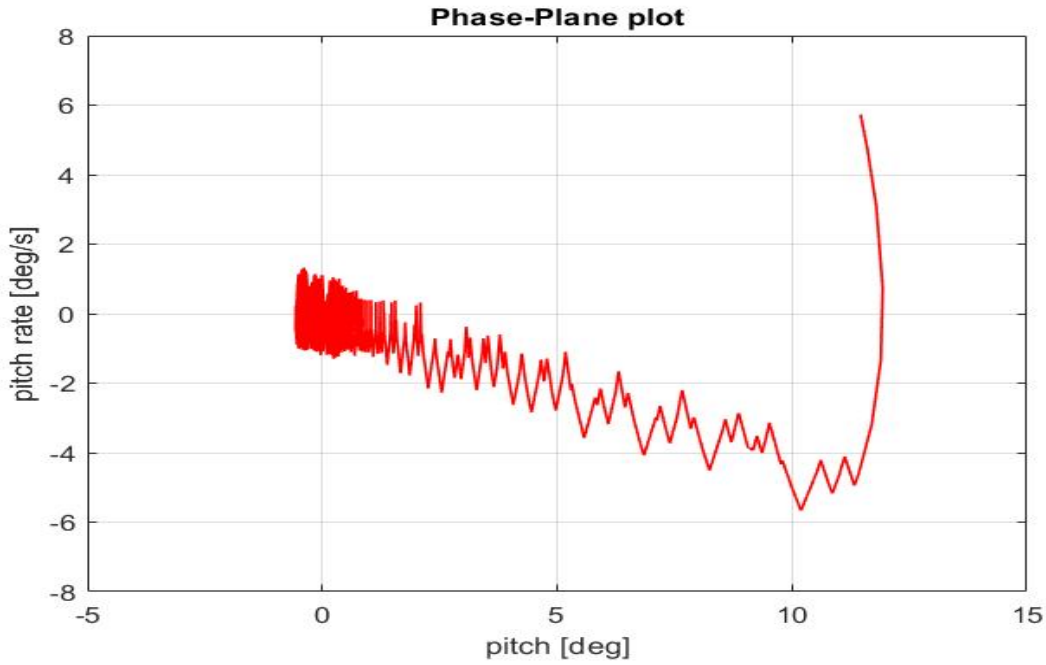

Figure 5.21: Chattered phase plane

From Figure 5.21 we can see the typical behaviour of a system under classic SMC. Starting from the initial condition, the controller take it on the sliding manifold and once started the sliding motion, the chattering phenomenon arises.

To avoid this problem, the sigmoid function method, described in section 4.3.2, has been applied.

The defined sigmoid function is the following:

$$sign(S) \approx \frac{S}{|S| + 0.1} \tag{5.13}$$

5.3.1 Ideal case

Considering a situation in which the only off-set present is on the pitch channel, with same initial conditions as table 5.2, and substituting the function defined in (5.13) inside the model, we get the following results:

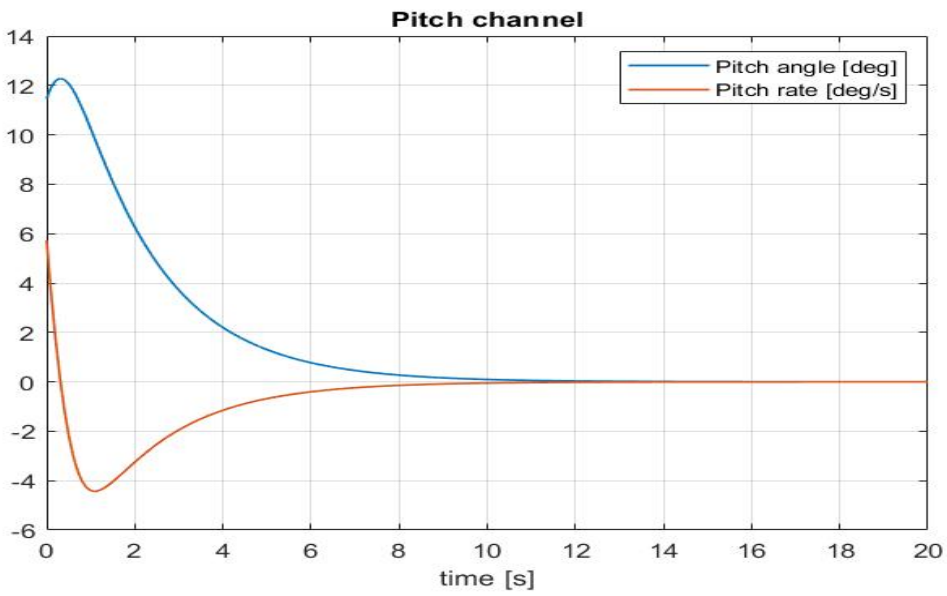

Figure 5.22: Pitch angle and pitch rate behaviour under sliding mode control

We can see, first of all, that the chattering phenomenon has been eliminated with the application of the sigmoid function. Furthermore, the damping of the motion is smoother with this kind of control than the one we got with the LQR. To obtain this trend, the gimbal offset angle needed is the following:

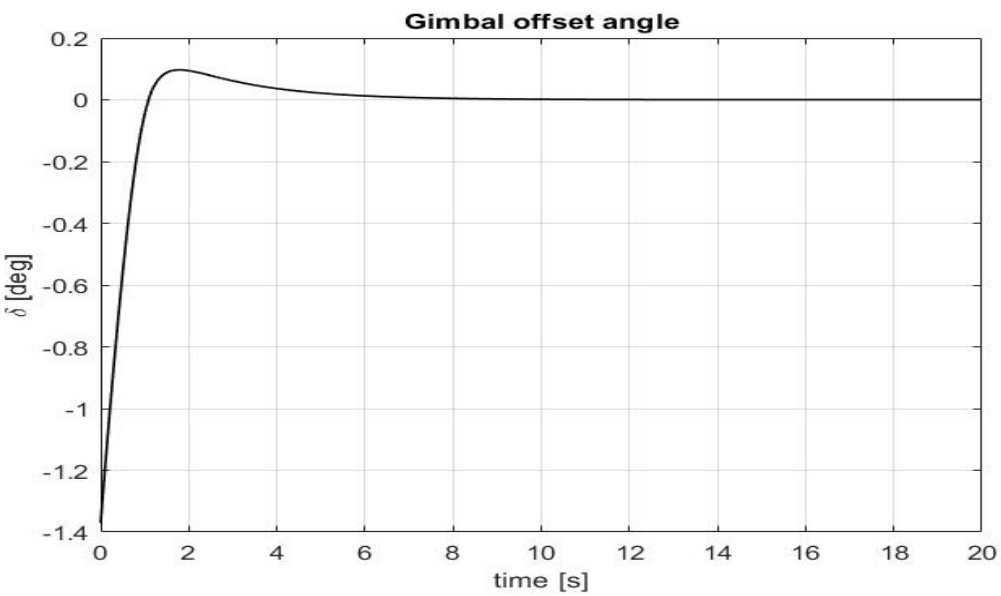

Figure 5.23: Angle δ under sliding mode control

Comparing again with the same situation in the LQR control case, we see that the smoother action needs a bigger control angle from the engine. However, even if there

is an increase, the angle is largely contained in the working range.

5.3.2 Perturbed case

To asses how the sliding mode control behaves under external disturbances, we start the analysis from the application of the half-sine impulse, as already done with the LQR controller. Applying two different pulses to the pitch and yaw motion, we have:

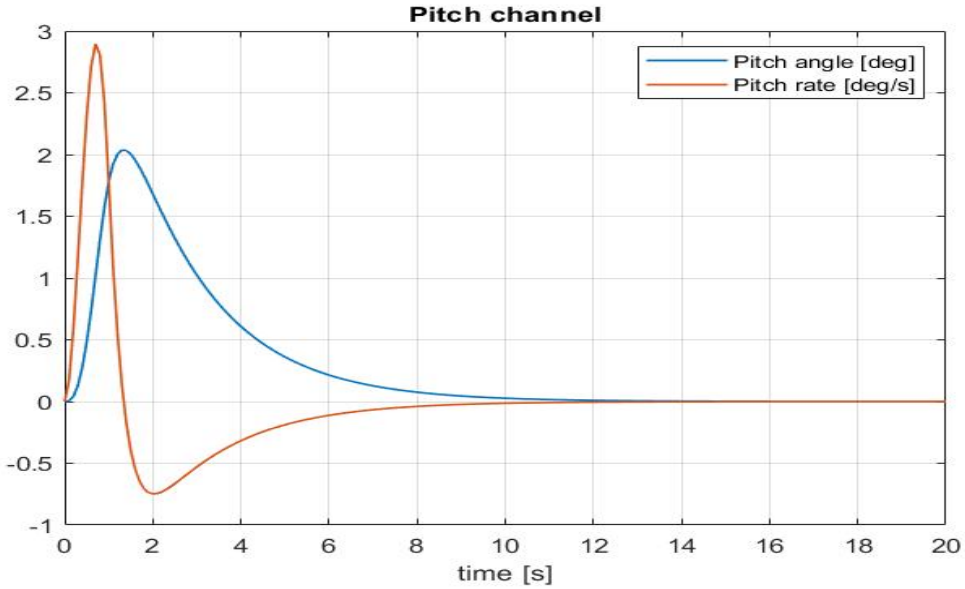

Figure 5.24: Pitch channel - impulse disturbance

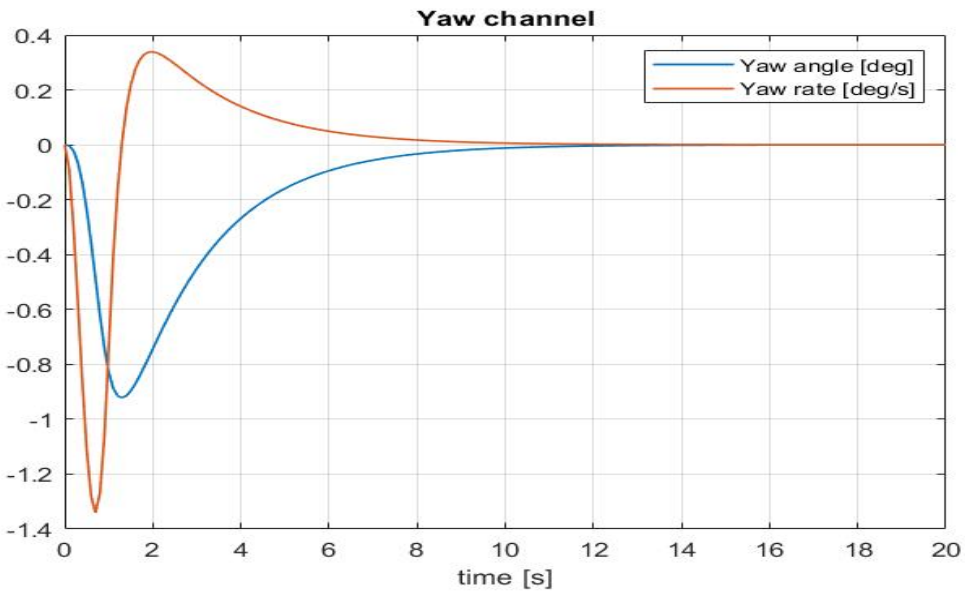

Figure 5.25: Yaw channel - impulse disturbance

From those graphs it is clear that, the sliding mode control presents an higher intrinsic robustness to external disturbances since the effect of the two pulses is more contained with respect to the disturbance generated compared to LQR control. Comparing the pitch channel, in fact, in the case of the LQR we have an angular displacement that reaches around 4° while, in the sliding mode control, the same pulse causes a displacement of about 2°. The actuation angles in this case are as depicted hereafter:

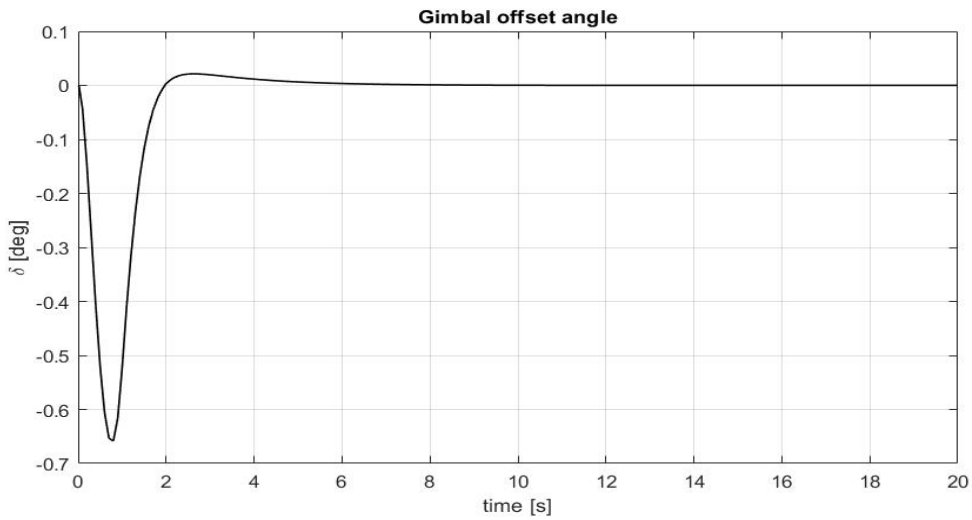

Figure 5.26: Gimbal offset angle - combined pulses disturbances

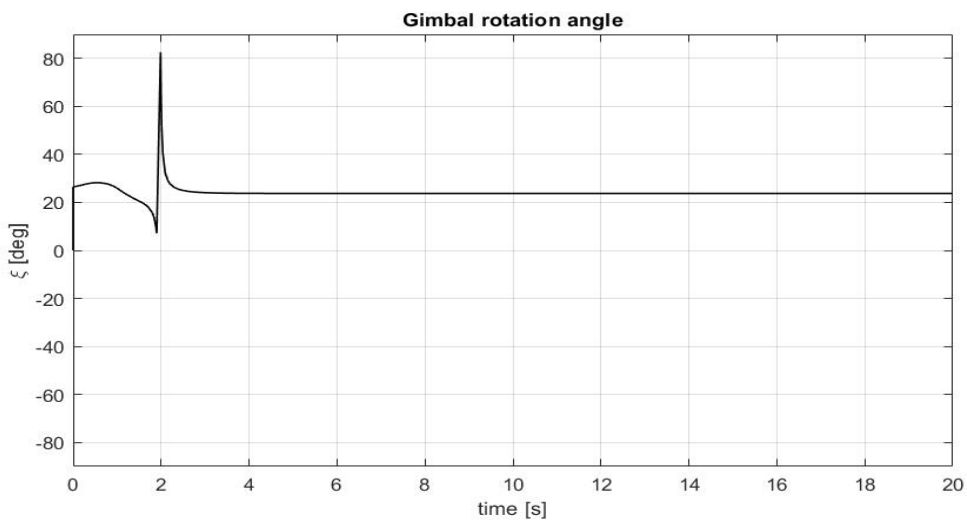

Figure 5.27: Gimbal rotation angle - combined pulses disturbances

Translating in terms of actuators displacement, we have:

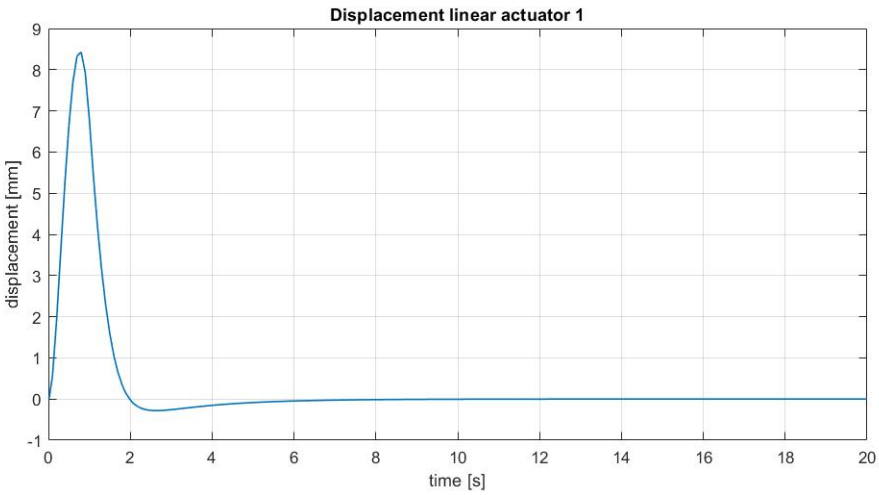

Figure 5.28: Displacement linear actuator 1 - pulse disturbance

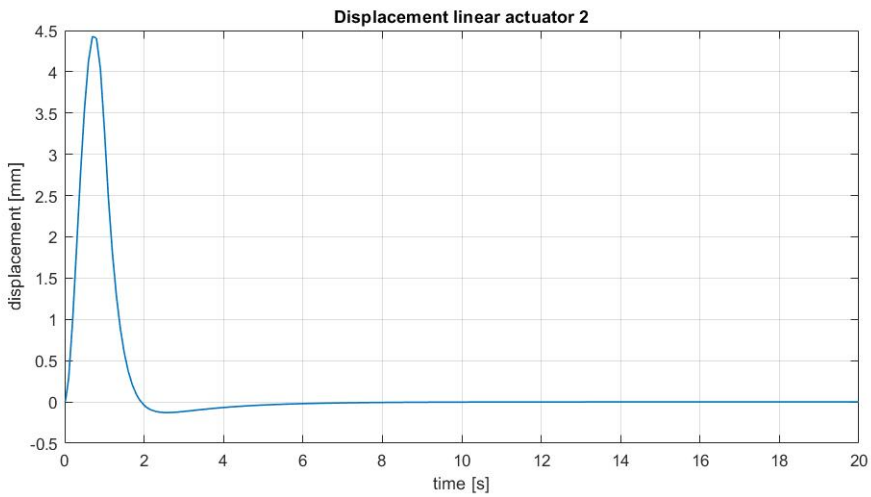

Figure 5.29: Displacement linear actuator 2 - pulse disturbance

The graphs above show that, in order to stabilize the system after the disturbance pulses, the maximum linear displacement, given by linear actuator 1, is around 9 mm. Given that the actuators speed is fixed at 30 mm/s, we see that this particular situation can be handled by the TVC system.

The second test, as for the case of the LQR system, is performed in terms of random noises. Also for the sliding mode control, the random noise generated is characterized by $RMS = 0.1$. With the linear quadratic controller, the angular displacements generated by this noise were close to 4°. Instead, the behaviour of the system under this perturbation, when a SMC system is applied, is the following:

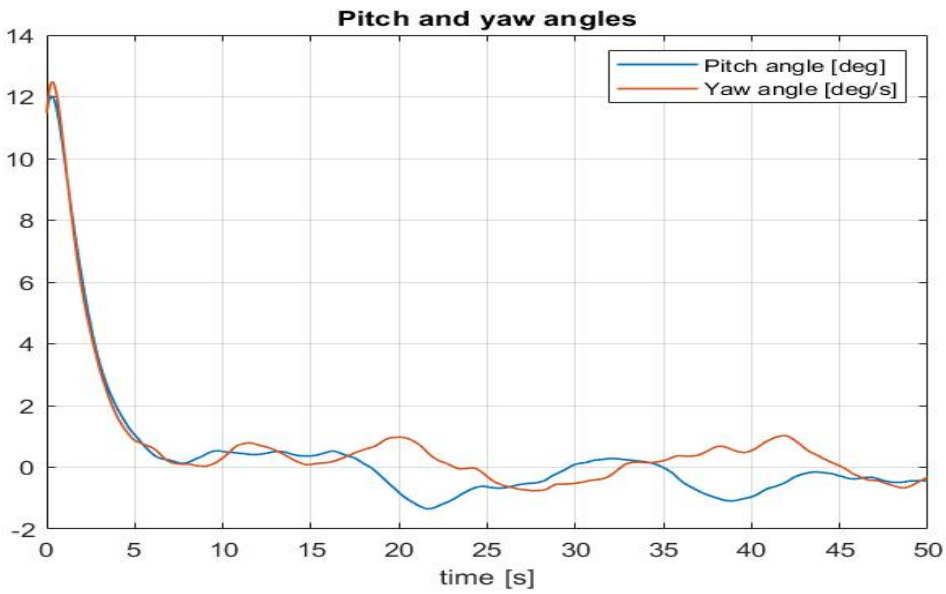

Figure 5.30: Pitch and yaw angles - random disturbance

We can see that, also in case of random noise, the higher robustness of the sliding mode controller is verified since the angular fluctuations are bounded between $-2°$ and $2°$. The performance of the latter could be even improved by increasing the gain k. However, increasing that constant, the gimbal offset angle used to balance the system would increase, decreasing consequently its range of applicability. Also in this case, the displacement requested to the actuators could lead to undesired issue:

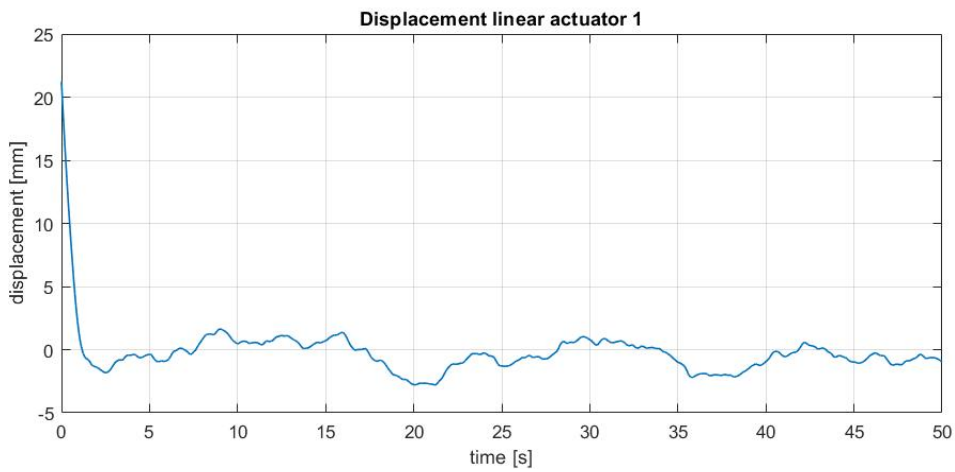

Figure 5.31: Displacement linear actuator 1 - random disturbance

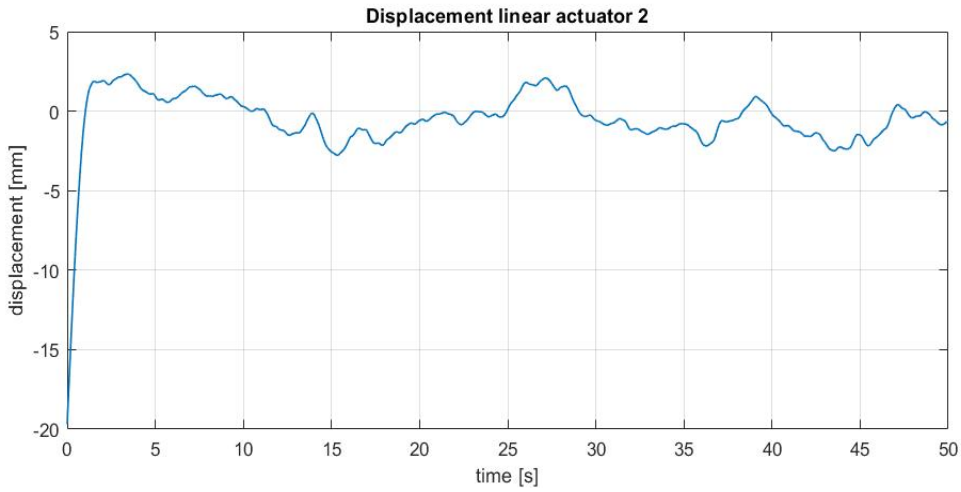

Figure 5.32: Displacement linear actuator 2 - random disturbance

Taking as example the pitch angle, we can see that the sliding mode controller shows a good response also to errors and disturbances in the state measurements:

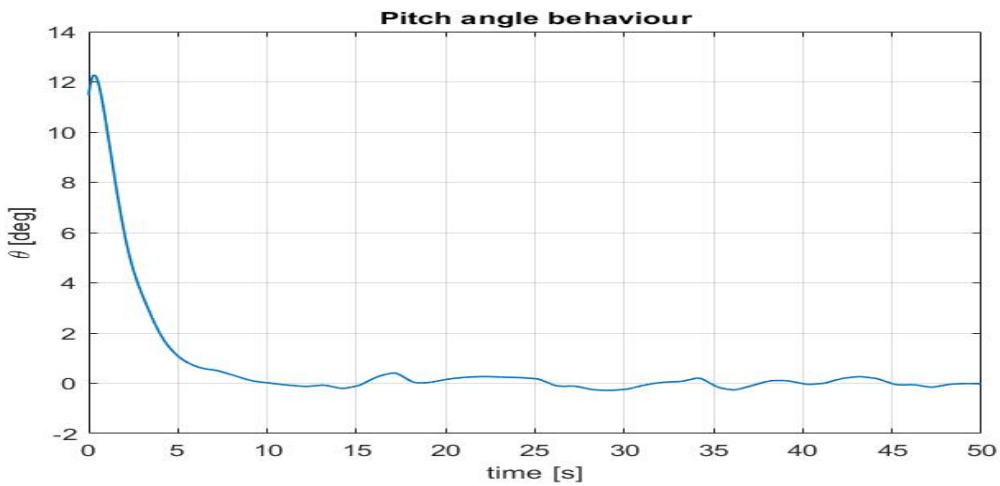

Figure 5.33: Pitch angle fluctuation due to measurements errors

To conclude the analysis, also in the case of the sliding mode controller, a set of 350 random initial conditions is generated in order to assess how effective can be the employment of the TVC system in the vehicle through a Monte Carlo simulation. To generate the random inputs, the same boundary conditions stated in (4.9) and (4.10) are imposed. The results of the simulation in terms of pitch angle, yaw angle and δ angle are shown below:

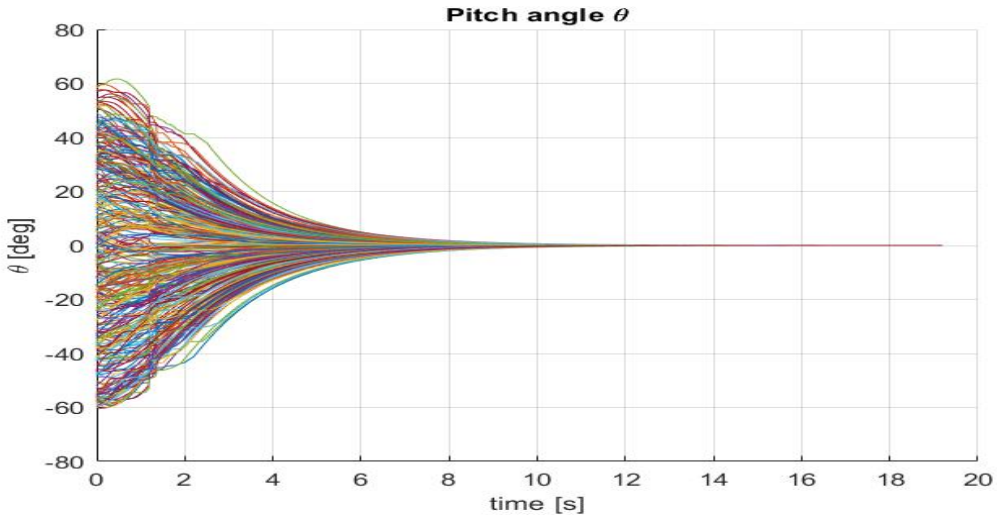

Figure 5.34: Pitch angle - different scenarios

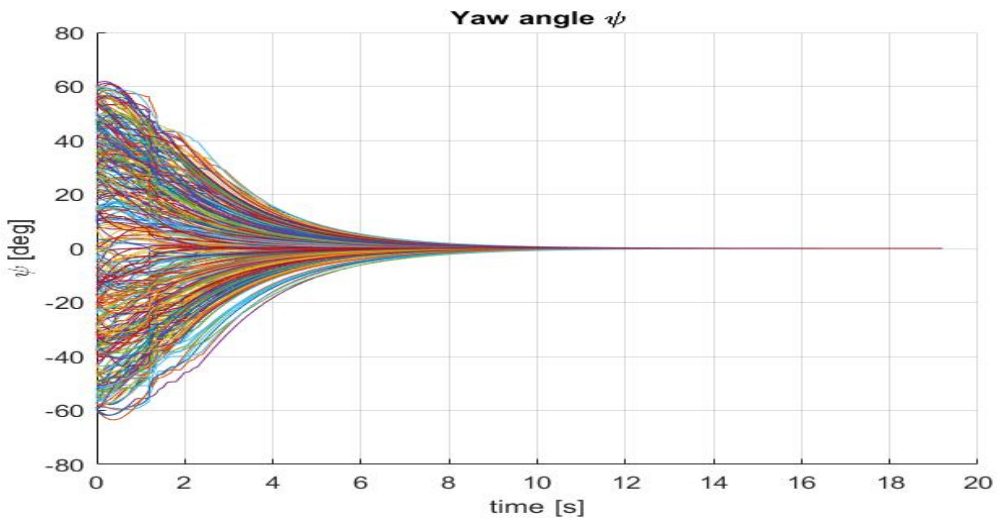

Figure 5.35: Yaw angle - different scenarios

We can see that, also the sliding mode control, for all the different scenarios generated, shows a good behaviour and a good damping of the initial off-set.

Concerning the gimbal off-set angle, we get the following results:

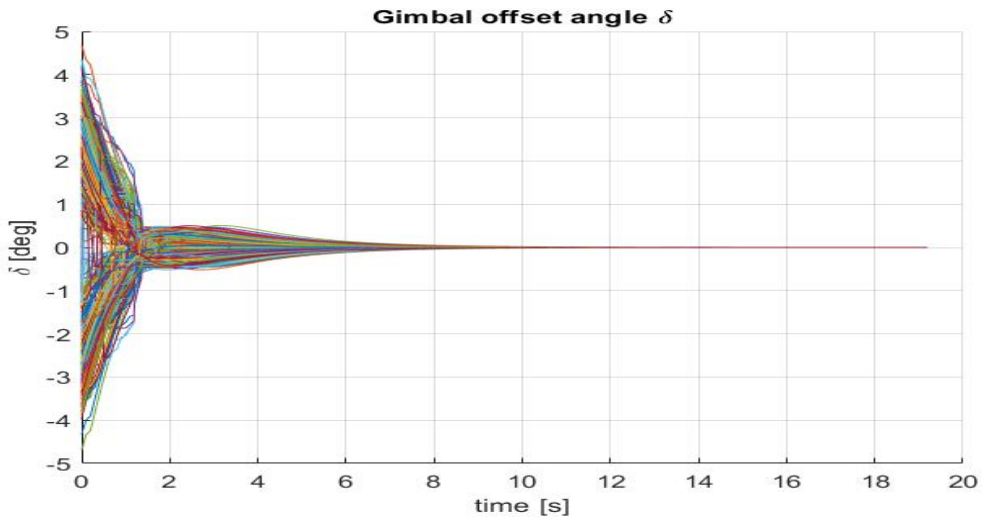

Figure 5.36: Gimbal offset angle - different scenarios

In general, during the analysis, the sliding mode control showed an higher robustness to external noise and disturbance, together with a very smooth damping of given off-set from the desired attitude. In general, the better response of the system was partnered by an higher value of gimbal angle needed to restore the desired condition. Nevertheless, the above simulations show that, even if we have a little increase of angle needed, the range predesignated for the TVC is widely satisfying the request of the control system. This is a nice result to underline. In fact, even if the cone of operation of the TVC system has been limited in order to have a faster actuation to control rapid unwanted attitude changes, this restricted range still allows a large number of maneuvers to be accomplished. However, as in the previous case, initial conditions outside the given boundary conditions could lead to exceed the cone of operation of the thrust vectoring system.

The synchronization between TVC and RCS systems is really important for the management of the dynamics of the vehicle. Due to lack of time this task couldn't be completed but, the main idea to get it that has been carried out is the implementation, inside the control logic, of a switcher block that manages the usage of the two different attitude control system. In particular, according to the torque needed to restore a particular condition to the desired one, the virtual gimbal offset angle needed to get that particular torque is calculated. If this angle is within the predefined range, the control torque is given by the TVC system otherwise, the switcher block commands to the RCS system to accomplish the attitude control.

Conclusions and future work

The aim of the presented work was the design and simulation of a thrust vectoring system for a lunar lander prototype vehicle using a jet turbine engine, on the LEAPFROG project. After the first phase that designed the hardware composing the required attitude control system definition, a linear quadratic regulator and a sliding mode controller were designed and both were analyzed regarding possible pros and cons of the application of each to a new TVC system. Results have shown that both controllers exhibited a good behaviour in presence of attitude off-set or low frequency disturbances. Good response have been verified also in presence of errors and noise in measurements. Concerning high frequency noise, both control systems have been affected by quite relevant angular displacement but, the sliding mode control presented a better behaviour to stabilize. My analysis was limited due to the relative lack of detailed engine dynamics and platform disturbances that could affect the prototype during a flight test. This leads the design of the final control system to be a bit harder since classical theory of linear systems can be applied per reasonable assumptions. One of them. for example, is the assumption of constant inertia that is needed to apply the reduced quaternion model. This hypothesis,in fact, makes the model unusable in case of long flight time that leads to potentially higher fuel consumption. A non-linear approach is for sure the best solution for the actual status of the vehicle, considering that the different parameters can be properly tuned according to the particular needs. The design of the presented thrust vectoring system is a large improvement for LEAPFROG since it can increase it's maneuverability and can reduce the usage of the cold gas thruster system. This TVC system can have a very good behaviour, for example, when a steering maneuver is needed during a flight trajectory or to keep the attitude in presence of some particularly high disturbances. However, the usage of the RCS system cannot be avoided since the actuation system used for the thrust vectoring still has some limitations. Moreover, the results given in chapter five are all related to short time flight conditions, in which the mass properties of the system can be considered constant. In case of long flight time, the propellant mass consumed by the engine becomes more and more important. This factor, combined to the particular placement of the tank for the engine fuel, would lead to a motion of the center

of mass towards the gimbal point, decreasing, consequently, the lever arm available for the control system. This reduction will lead to an increase of the tilting angle of the engine needed, making the TVC less applicable. Sliding mode control does give a good starting point for the synchronization of the TVC and the RCS system, since the control system, according to the distance between the actual and the desired position, calculates the control torques needed to achieve the goal. These torques can be then used to determine which system, ie TVC or RCS or both, would use the torques themselves to provide for attitude control.

Future work that will be needed to improve the quality of the control system, are the assessment of the real properties of the actuators through lab testing and an analysis of the behaviour of the prototype under particular atmospheric conditions. Moreover, the designed control system should be updated with the actual mass properties once the full vehicle is totally built. A mass variation model should also be considered when long flight times are taken into account.

Appendix A

Lyapunov stability theorem

Consider a non-linear, time invariant system described by the following set of differential equations:

$$\dot{x} = f(x, u) \tag{A.1}$$

where u is the set of available control inputs. Let's assume that x_T is an equilibrium point for the system (i.e. $f(x_T) = 0$). Let's also define a candidate Lyapunov function $V(x)$ such that:

- $V(x_T) = 0$
- $V(x) > 0$ for each $x \neq x_T$
- $V(x) \to \infty$ if $x \to \infty$

Lyapunov's stability theorem states that, defined a scalar potential function V, which is continuous and with a global minimum at the target state (x_T), the system described by (A.1) converges to the goal point if the rate of change of the potential is negative definite. In essence, Lyapunov's theorem guarantees that the closed loop system is globally asymptotically stable in x_T if [22]:

$$\dot{V}(x) = \frac{dV}{dx}\frac{dx}{dt} = \frac{dV}{dx} f(x, u) < 0 \ for \ x \neq x_T \tag{A.2}$$

Bibliography

[1] Martin Marietta Aerospace. Titan iiie/centaur d-it systems summary. 1973.

[2] JetCat Americas. *JetCat PRO Engines datasheet*, 2017 edition.

[3] H Alemi Ardakani and TJ Bridges. Review of the 3-2-1 euler angles: a yaw-pitch-roll sequence. *Department of Mathematics, University of Surrey, Guildford GU2 7XH UK, Tech. Rep*, 2010.

[4] Andrew Ball, James Garry, Ralph Lorenz, and Viktor Kerzhanovich. *Planetary landers and entry probes*. Cambridge University Press, 2007.

[5] David Barnhart, Joseph Sullivan, Peter Will, and Mike Gruntman. Advancing exploration risk reduction and workforce motivation through dynamic flight testing. In *AIAA SPACE 2007 Conference & Exposition*, page 6040, 2007.

[6] Mehmet Cem Catalbas and Arif Gulten. A novel approach for optimization of nozzle angle and thrust vectoring controller via a sub-mutation genetic algorithm. *Int. J. Innovative Comput. Inf. Control*, 13(6):1929–1940, 2017.

[7] Huiping Chu, Lin Ma, Kexin Wang, Zhijiang Shao, and Zhengyu Song. Trajectory optimization for lunar soft landing with complex constraints. *Advances in Space Research*, 60(9):2060–2076, 2017.

[8] JR Cowan and Rae Ann Weir. Design and test of electromechanical actuators for thrust vector control. 1993.

[9] Taw Dwyer III and Al Batten. Exact spacecraft detumbling and reorientation maneuvers with gimbaled thrusters and reaction wheels. 1985.

[10] Clint Ensworth. Thrust vector control for nuclear thermal rockets. In *49th AIAA/ASME/SAE/ASEE Joint PropulsionConference*, page 4075. 2013.

[11] Andrew B Facciano, Paul Lehner, and Wayne N Anderson. Dissolvable thrust vector control vane, April 15 2003. US Patent 6,548,794.

[12] Murat Furat and İlyas Eker. Experimental evaluation of sliding-mode control techniques. *Çukurova Üniversitesi Mühendislik-Mimarlık Fakültesi Dergisi*, 27(1):23–37, 2012.

[13] Rozaimi Ghazali, Yahaya Md Sam, Mohd Fua'Ad Rahmat, Abd Wahab Ishari Mohd Hashim, et al. Performance comparison between sliding mode control with pid sliding surface and pid controller for an electro-hydraulic positioning system. *International Journal on Advanced Science, Engineering and Information Technology*, 1(4):447–452, 2011.

[14] CJ Green and Foy McCullough Jr. Liquid injection thrust vector control. *AIAA Journal*, 1(3):573–578, 1963.

[15] J Guldner and VI Utkin. The chattering problem in sliding mode systems. In *Fourteenth Intenational Symposium of Mathematical Theory of Networks and systems, MTNS2000*, 2000.

[16] Morgan Hendry, Kristina Rojdev, Jason Cheng, Omer Faghfoor, Alvin Garcia, Paul Giuliano, Lucy Hoag, Cassandra Raskin, Michael Ruldolph, and Omair Rahman. Leapfrog: Lunar entry and approach platform for research on ground. In *AIAA Infotech@ Aerospace 2007 Conference and Exhibit*, page 2764, 2007.

[17] Hiranya S Jayakody. Robust control of vectored thrust aerial vehicles via variable structure control methods. 2016.

[18] Yunhua Li, Hao Lu, Shengli Tian, Zongxia Jiao, and Jian-Tao Chen. Posture control of electromechanical-actuator-based thrust vector system for aircraft engine. *IEEE Transactions on Industrial Electronics*, 59(9):3561–3571, 2011.

[19] Leandro R Lustosa, Flávio Cardoso-Ribeiro, François Defaÿ, and Jean-Marc Moschetta. A new look at the uncontrollable linearized quaternion dynamics with implications to lqr design in underactuated systems. In *2018 European Control Conference (ECC)*, pages 3120–3125. IEEE, 2018.

[20] Gene J Matranga, Wayne Ottinger, and Calvin R Jarvis. *Unconventional, Contrary, and Ugly: The Lunar Landing Research Vehicle*. National Aeronautics and Space Administration, NASA History Division, 2006.

[21] Donald McLean. Automatic flight control systems. *Measurement and Control*, 36(6):172–175, 2003.

[22] Dario Modenini and Paolo Tortora. *Lecture Notes in Spacecraft Attitude Dynamics and Control*.

[23] RM Murray. Control and dynamical systems. *California Institute Of Technology*, 2009.

[24] United performance metal. *6061 Aluminum datasheet.*

[25] M Ryan Schaefermeyer. Aerodynamic thrust vectoring for attitude control of a vertically thrusting jet engine. 2011.

[26] Richard H Sforzini. Derivation of the thrust equation from conservation of energy. *Journal of Aircraft*, 7(6):538–541, 1970.

[27] Yuri Shtessel, Christopher Edwards, Leonid Fridman, and Arie Levant. *Sliding mode control and observation.* Springer, 2014.

[28] Vaibhav Singal, Jash Bajaj, Nimish Awalgaonkar, and Sarthak Tibdewal. Cfd analysis of a kerosene fuel tank to reduce liquid sloshing. *Procedia Engineering*, 69:1365–1371, 2014.

[29] Jean-Jacques Slotine and S Shankar Sastry. Tracking control of non-linear systems using sliding surfaces, with application to robot manipulators. *International journal of control*, 38(2):465–492, 1983.

[30] Jean-Jacques E Slotine, Weiping Li, et al. *Applied nonlinear control*, volume 199. Prentice hall Englewood Cliffs, NJ, 1991.

[31] Barton H Snow. Thrust vectoring control concepts and issues. *SAE transactions*, pages 1488–1499, 1990.

[32] William S Widnall. The minimum-time thrust-vector control law in the apollo lunar-module autopilot. *IFAC Proceedings Volumes*, 3(1):136–153, 1970.

[33] Windynation. *Actuators user manual.*

[34] Yaguang Yang. Quaternion based model for momentum biased nadir pointing spacecraft. *Aerospace Science and Technology*, 14(3):199–202, 2010.

[35] Yaguang Yang. Analytic lqr design for spacecraft control system based on quaternion model. *Journal of Aerospace Engineering*, 25(3):448–453, 2012.

[36] Fu-Kuang Yeh, Kai-Yuan Cheng, and Li-Chen Fu. Rocket controller design with tvc and dcs. In *Proceedings of the 2003 American Control Conference, 2003.*, volume 2, pages 1655–1660. IEEE, 2003.

[37] Jean Zyla. *Attitude control system for Lunar Lander simulator.* University of Southern California, 2019. Summer work report.

Acknowledgements

Vorrei ringraziare, innanzitutto, il Prof. Marco Zannoni e il Prof. Paolo Tortora per la loro disponibilità e per l'aiuto datomi nel trovare la possibilità di svolgere la tesi all'estero.

Many thanks to Prof. David Barnhart, to the entire SERC and in particular to LEAPFROG team for the chance to work in a great environment and meet wonderful people. I had a really good time and it was a great pleasure working with you. I'll miss you guys.

To everyone I met in Los Angeles, happy and glad to have friends on the other side of the world.

Un grazie ai miei amici di sempre per le cene, le serate e tutti i momenti spensierati. Le birre bevute con voi hanno sempre avuto un altro sapore!

Grazie a Virginia, che mi è stata sempre accanto, dall'inizio e nonostante tutto, dandomi forza nei momenti più difficili, in particolare durante il lavoro di tesi.

Grazie a Claudio, Vania, Ilaria, Alessandro, ai bimbi e a tutta la mia famiglia per tutto il sostegno che mi avete dato e per aver sempre creduto in me durante questo percorso, a volte anche più di quanto facessi io stesso.

Un grazie a mio nonno, che in me ci ha creduto anche prima che questo percorso fosse iniziato. So che si sei sempre stato!

Infine, un ringraziamento speciale ai miei genitori. Mi avete sempre supportato in ogni mia scelta, dandomi l'occasione di fare una delle esperienze più belle che potessi desiderare. Spero, un giorno, di riuscire a restituirvi anche solo un decimo di quello che mi avete sempre dato. Tutto quello che sono stato, che sono e che sarò lo devo a voi. Grazie!